DEM study of particle scale and penetration rate on the installation mechanisms of screw piles in sand

Cerfontaine, B.; Ciantia, M.; Brown, M. J.; Sharif, Y. U.

Published in:
Computers and Geotechnics

DOI:
10.1016/j.compgeo.2021.104380

Publication date:
2021

Computers and Geotechnics 139 (2021) 104380

Contents lists available at ScienceDirect

Computers and Geotechnics

journal homepage: www.elsevier.com/locate/compgeo

DEM study of particle scale and penetration rate on the installation mechanisms of screw piles in sand

B. Cerfontaine [a,*], M. Ciantia [b], M.J. Brown [b], Y.U. Sharif [b]

[a] Engineering and Physical Sciences, University of Southampton, Boldrewood campus, Southampton, UK
[b] School of Science and Engineering, University of Dundee, Fulton Building, Dundee DD1 4HN, UK

ARTICLE INFO

Keyword:
Screw Piles
Anchors
Discrete Element Method (DEM)
Helical Piles

ABSTRACT

Screw piles are efficient anchors to sustain large uplift loads and can be installed with low noise or vibration. Screw piles dimensions are currently increasing, renewing research interest to reduce the installation requirements (torque and crowd or vertical force). The Discrete Element Method (DEM) is an ideal technique to investigate the complex soil behaviour during screw pile installation. Different techniques such as particle upscaling or increase of pile penetration rate have been used to reduce the CPU time to more acceptable durations (e.g. few days or weeks). This paper investigates how such techniques can affect the accuracy of the results and change the installation mechanisms. Results show that maintaining a low particle scaling factor is essential to reproduce the correct mechanism at low pile advancement ratio (AR, defined as the vertical displacement per rotation divided by the helix pitch). The pile overflighting ($AR \leq 1$) creates an upwards movement of particles, which in turn creates some tension in the pile. Smaller advancement ratios require smaller particles to accurately capture this effect. Results also show that the pile penetration rate must be maintained relatively low to avoid spurious inertial effects.

1. Introduction

Screw (or helical) piles are composed of one or several steel helices connected to a shaft (Perko, 2009). They are screwed into the ground by applying a torque at the top of the pile together with a compressive (crowd) force. This technology was invented in the 19th century to found lighthouses (Lutenegger, 2011) and has been used onshore since to anchor relatively light structures such as telecommunication towers (Schiavon et al., 2016a). Screw pile helices have two purposes. They provide a significant uplift resistance once installed (Stanier et al., 2014; Giampa et al., 2017; Hao et al., 2019; Cerfontaine et al., 2020) and the helix rotation provides some pull-in force which facilitates pile installation (Cerfontaine et al., 2021). This "silent" installation mode, with low noise or vibration, makes them suitable for offshore applications (Byrne and Houlsby, 2015; Davidson et al., 2020; Spagnoli et al., 2020) or foundation in urban areas (Choi et al., 2013). More recent applications show an increase in pile dimensions (Tang and Phoon, 2020) to act as foundations for buildings (Komatsu, 2007), bridges (Harnish and El Naggar, 2017) or modern offshore energy applications (Byrne and Houlsby, 2015; Spagnoli et al., 2020). Consequently, novel design and modelling methods are necessary to estimate the installation requirements, design appropriate installation plant and to ensure that early refusal will not occur.

The Discrete Element Method (DEM) is widely used to investigate granular material behaviour at the element scale as it offers readily accessible information at the micro-scale, which may be used to uncover relevant micromechanics (Da Cruz et al., 2005; Khoubani and Evans, 2018; Shire et al., 2021). Recently, the DEM has proven to be suitable also for the modelling of penetration problems such as cone penetration resistance (Arroyo et al., 2011; Zhang and Wang, 2015), large pile jacking (Sharif et al., 2020b) or small scale pile penetration (Ciantia et al., 2019). Particle upscaling, where dimensions of simulated particles are larger than their real size is commonly used to reduce simulation CPU costs, while still capturing the correct macroscopic behaviour being simulated. The same scaling factor (SF) can be applied to all particles (Arroyo et al., 2011; Coetzee, 2019; Zhang and Evans, 2019) or vary by zones (McDowell et al., 2012; Sharif et al., 2020b). Scaling factors of 25–50 have previously been used to simulate CPT penetration (Arroyo et al., 2011; Ciantia et al., 2016) where values of pile diameter (D_s) to average particle size (d_{50}) usually ranges from 2.4 to 12 (Khosravi et al., 2020). Scaling factors of 15 and 20 were used to simulate continuous

* Corresponding author.
E-mail addresses: b.cerfontaine@soton.ac.uk (B. Cerfontaine), m.o.ciantia@dundee.ac.uk (M. Ciantia), m.j.z.brown@dundee.ac.uk (M.J. Brown), y.u.sharif@dundee.ac.uk (Y.U. Sharif).

https://doi.org/10.1016/j.compgeo.2021.104380

Available online 20 August 2021

Nomenclature

AR	Advancement ratio
d_{50}	Average particle size
d_{100}	Maximum particle size
D_h	Helix diameter
D_r	Relative density
D_{rev}	Diameter of the representative elementary volume
D_s	Shaft diameter
D_{sb}	Diameter of the soil bed
F_b	Resultant force acting on the base
F_h	Resultant force acting on the helix
F_s	Resultant force acting on the shaft
F_z	Total vertical force
G_{sand}	HST95 sand shear modulus
H	Embedment depth of the pile
H_{rev}	Diameter of the representative elementary volume
H_{sb}	Height of the sand bed
I	Inertial number
M_s, M_d	Material parameter (exponent) of the contact model
N	Model scaling factor due to enhanced gravity
n	Porosity
n_{av}	Average porosity of the sand bed
$N_{particles}$	Number of particles
N_γ	Bearing capacity factor
N_q	Bearing capacity factor
$p_0^{'}$	Average effective confining stress
p_h	Helix pitch
T_b	Torque acting on the base
$T_{c\text{-}e}$	Torque contribution of the cutting edge
t_h	Helix plate thickness
T_h	Resultant torque acting on the helix
T_s	Resultant torque acting on the shaft
T	Total torque
SF	Particle scaling factor
v_{tot}	Total particle velocity
v_{ref}	Reference penetration rate profile (I = 0.01)
v_z	Vertical penetration rate of the pile during installation
$v_{z,10}$	Vertical penetration rate profile, for SF = 10, AR = 0.5 and I = 0.01.
$v_{z,max}$	Maximum penetration rate assumed to maintain quasi-static conditions
z	Depth
z_{min}	Minimum depth of a sampling box
z_{max}	Maximum depth of a sampling box
β	Material parameter
$\dot{\gamma}$	Shear strain rate
Δz_h	Vertical displacement of the helix after one helix revolution
Δ_h	Displacement of particle in the horizontal plane
Δ_x,Δ_y,Δ_z	Particle displacement in x, y or z direction
η	Average mechanical ratio
η_p	Particle mechanical ratio
ρ	Radial coordinate
ρ_{min}	Minimum radial coordinate of a sampling box
ρ_{max}	Maximum radial coordinate of a sampling box
ρ_s	Particle density
ω	Pile rotation rate during installation

thread (Shi et al., 2019) or single helix (Sharif et al., 2020a) screw piles installation respectively. In all cases, enough particles must be used to ensure the soil response is scale independent. Scaling issues have been reported when particle size increases, such as modification of shear band geometry in triaxial tests (Badakhshan et al., 2020), reduction in wall limit pressure during cavity expansion (Dong et al., 2018) or increase in wedge-shaped tool penetration resistance (Lommen et al., 2019).

The influence of the particle scaling on the results is a function of the relative dimension of the modelled structure and the particle size, but it is mainly dependent on the dominant physical mechanism. The penetration mechanism of screw pile is related to their advancement ratio (AR) during installation (Bradshaw et al., 2018)

$$AR = \frac{\Delta z_h}{p_h} \tag{1}$$

defined as the vertical displacement per helix rotation (Δz_h), divided by the helix pitch (p_h, Fig. 1a). Standards recommend that the AR should be equal to 1 ± 0.15 (BS8004:2015, 2015), which is termed pitch-matched installation. However, ensuring this condition can require a large crowd force for larger piles, which may be impractical to apply in the field (Davidson et al., 2020). Contrary to current industry guidance, recent centrifuge (Cerfontaine et al., 2021), DEM (Sharif et al., 2019) and 1g small-scale testing (Wang et al., 2020) have shown that installation of screw piles in sand at lower AR (<0.8) reduced the crowd force

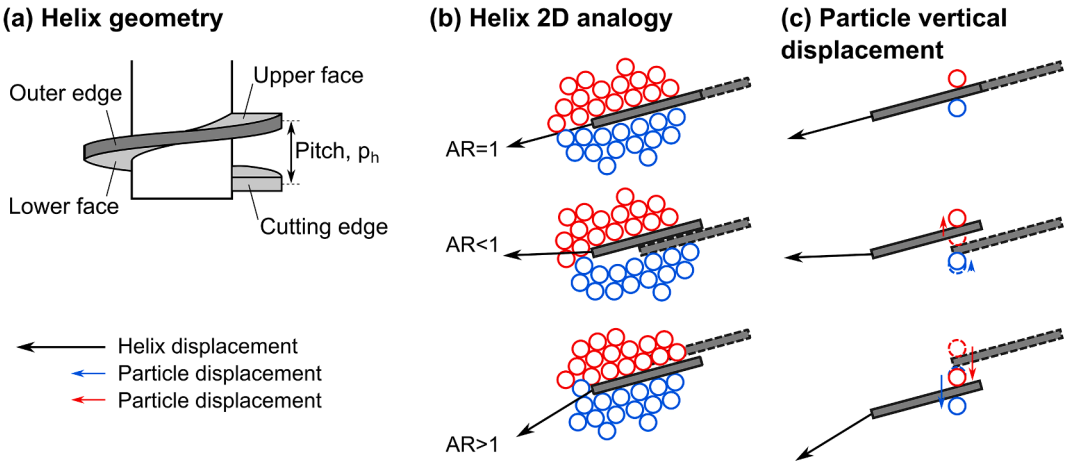

Fig. 1. Helix geometry and 2D analogy of the installation: (a) Details of helix geometry; (b) Advancement ratio (AR) effect on the helix displacement (black arrow) and soil mass; (c) Single particle vertical displacement (coloured arrows) as a function of AR.

and could enhance the uplift capacity. Installation with AR < 1 is referred to as overflighting.

Fig. 1b idealises the helix behaviour in 2D as a function of the AR. It is based on results from the authors interpretation of geotechncial centrifuge (Cerfontaine et al., 2021) and DEM results (this paper). For AR = 1, the helix displacement is aligned with the helix geometry and particles are slightly displaced on both sides of the plate during penetration (Fig. 1b). A particle in contact with a helix face, and whose horizontal displacement is fixed, remains unaffected by its movement (Fig. 1c). For AR < 1, the helix vertical displacement is lower than p_h for each rotation. The helix movement is downwards (Fig. 1b), but it tends to move particles upwards (Fig. 1c). For AR greater than 1, both helix and particle movements are oriented downwards. Obviously, the 3D behaviour of the helix and its interactions with the pile shaft create a more complicated behaviour. A limited number of studies have investigated different geometries of screw piles with the DEM (Tan et al., 2011; Chen et al., 2018; Shi et al., 2019; Sharif et al., 2020a), but the influence of the particle scaling and penetration rate on the different mechanisms has not been investigated in the literature.

The goal of this paper is to identify the main installation mechanisms of (overflighted) screw piles and investigate the effect of numerical parameters (particle upscaling or penetration rate) on their observed behaviour. The first objective is to describe the basic mechanism of the overflighting process, in order to inform experimental results and design methods. The second objective is to provide guidance for future simulations to ensure that accurate results are obtained, while the CPU time remains acceptable. Three particle scaling factors, three pile installation velocities and two advancement ratios were tested in 9 simulations. Numerical results are validated against previous geotechnical centrifuge experimental results (Cerfontaine et al., 2021).

2. Methodology

PFC3D 6.00.17 (Itasca Consulting Group, 2019) was used to create three soil beds of increasing particle sizes, but at the same relative density.

2.1. Screw pile model

The model pile is shown in Fig. 2. The helix (D_h) and shaft (D_s) diameters were respectively 21.25 mm and 11 mm (1.06 m and 0.55 m at prototype scale). The helix plate was 1.4 mm (0.07 m at prototype scale). The pile behaviour is rigid, and it is installed by specifying rotation and vertical displacement rates along its axis. The base is closed-ended to match centrifuge previous centrifuge modelling (Cerfontaine et al., 2021), described in section 2.6.

2.2. Soil bed preparation

The DEM was used to create a virtual centrifuge environment with an enhanced gravity (model scaling factor N = 50g, with g the acceleration of gravity) to mimic the conditions of centrifuge tests used for validation (see section 2.6). Three scaling factors (SF = 10, 15, or 20) were selected to investigate the particle scale effect, while maintaining reasonable simulation times (below 3 weeks per simulation, computers specifications: Intel® Xeon® CPU E5-1650 v4 @3.60 GHz, 48 GB RAM, 64-bit operating system). Each SF was applied to the particle size distribution (PSD) of the HST95 sand (properties in Table 1, after Lauder (2010) and Sharif et al., (2019)) to create a polydisperse sample. The particle-cell replication method (PCRM), proposed by Ciantia et al. (2018), was used to create the soil bed from a representative elementary volume (REV) at a target porosity of 0.38. The same porosity corresponds to a relative density D_r = 52% of the HST95 sand material, as per the centrifuge tests. A homogeneous sand bed was created to match centrifuge test conditions and simplify the interpretation of results. Seven REVs were piled to create the final soil bed. The initial stress state corresponds to a coefficient of earth pressure at rest (K_0 = 0.47). The gravity was enhanced to 50g to correspond to the centrifuge test conditions. The initial contact forces were scaled to correspond to this gravity field, as described in (Ciantia et al., 2018). The three samples took between half a day (SF = 20) and two days (SF = 10) to create (Table 2).

The diameter of the soil bed (D_{sb} in Table 3) is smaller than the distance between the pile and boundary in the centrifuge experiment. It was chosen to reduce this dimension to reduce the number of particles and computational cost. The boundary was set up at a distance where particle radial displacement would be expected if the sand bed were semi-infinite. If a fixed displacement (infinite stiffness) wall had been used as a boundary condition, the radial stress field created by the restrained radial movement would have been greater than in reality (Khosravi et al., 2020). On the contrary, a constant pressure (zero stiffness) boundary condition would have led to the underestimation of the radial stress field because of the unrestrained movement of particles. Consequently, a constant stiffness boundary condition was imposed to reduce the potential boundary effects. Seven cylindrical rings, represented in Fig. 3, were associated with radial stiffnesses increasing with depth to match experimental conditions. The radial displacement (u_ρ) of each cylinder is servo-controlled with respect to its current radial position (ρ_{wall}) and is calculated based on elastic cavity expansion (Yu, 2000)

Table 1
HST95 sand physical properties, after (Lauder, 2010; Al-Defae et al., 2013).

Physical properties [unit]	Symbol	Value
Minimum void ratio [-]	e_{min}	0.467
Maximum void ratio [-]	e_{max}	0.769
Critical state friction angle [°]	ϕ	32
Sand-steel friction coefficient [°]	δ	24
Particle dimension [mm]	D_{10}	0.09
Particle dimension [mm]	D_{50}	0.141
Particle dimension [mm]	D_{100}	0.213
Particle density [kg/m^3]	ρ_s	2650
Sand shear modulus [MPa]	G_{sand}	$= 17.3\left(\frac{p'}{100}\right)^{0.548}$
Coefficient of earth pressure at rest	K_0	0.47

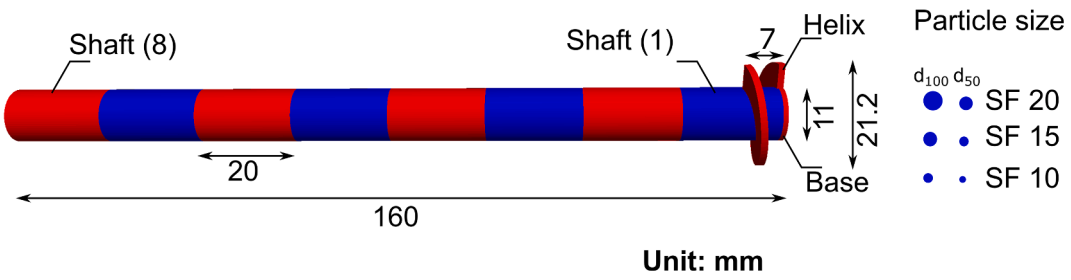

Fig. 2. Pile model and comparison with the particle size at three scaling factors (rotated through 90° in the figure, pile dimensions in mm).

Table 2
Soil bed characteristics, CPU time necessary between few hours to one day.

SF [-]	$N_{particles}$ [-]	n_{av} [-]	Duration[h]
10	632,305	0.38	12 h-36 h
15	187,330	0.38	
20	78,657	0.38	

Table 3
Soil bed and pile dimensions at prototype scale.

	Parameter [unit]	Symbol	Value
REV	Diameter [m]	D_{REV}	4.25
	Height [m]	H_{REV}	1.5
Soil bed	Diameter [m]	D_{sb}	4.25
	Height [m]	H_{sb}	10.50
Pile	Helix diameter [m]	D_h	1.06
	Shaft diameter [m]	D_s	0.55
	Helix thickness [m]	t_h	0.07
	Helix pitch [m]	p_h	0.35

$$u_\rho = \frac{\sigma_r - \sigma_{r,0}}{2G_{sand}}\rho_{wall} \tag{2}$$

where σ_r is the current average radial stress acting on the cylinder, $\sigma_{r,0}$ is the far field undisturbed radial stress and G_{sand} is the shear modulus of the sand. Both the far field radial stress and the sand stiffness are calculated at mid-depth of each cylindrical ring based on the parameters from Table 3.

Virtual sampling boxes defined by vertical ($z_{min} \leq z \leq z_{max}$) and radial ($\rho_{min} \leq \rho \leq \rho_{max}$) coordinates were created to assess the sample quality. For each square box ($\rho_{max} - \rho_{min} = z_{max} - z_{min} = 0.3m$), it is possible to calculate an average porosity and stress state based on the information carried by enclosed particles. The porosity (n) distribution is depicted for all soil beds in Fig. 4a along the vertical direction. The repeated pattern is due to the stacking of the 7 REVs to create the final soil bed (PCRM). The slight porosity inhomogenity in the REV along the vertical direction is simply replicated over the sand bed depth. This inhomogeneity will be further averaged by the installation process and has only a limited effect on the results. The greatest variation of porosity from minimum to maximum value is for the largest SF (20) and is equal to 0.01 (~8% D_r variation for HST95). The probability distribution of porosity is depicted in Fig. 4b and shows that the porosity is relatively homogeneous and slightly denser than the target porosity of the centrifuge experiments. The radial (σ_r) and vertical (σ_z) initial stress distributions are calculated similarly and show good homogeneity relatively close to the target (Fig. 4c).

Non-dimensional pile dimensions to particle size ratios are given in Table 4. The shaft (D_s) to average particle (d_{50}) diameter ratio ranges between 3.9 and 7.8. The space available between the two edges of the helix ($p_h - t_h$) is larger than the largest particle diameter (d_{100}). The effective radius ratio ($w_h = (D_h - D_s)/(2d_{50})$, after Schiavon et al. (2016b)), is greater than one, which ensures that there is more than one particle in contact over the width of the helix.

Finally, the installation mode of the helix is likely to introduce some additional particle scale effect. The vertical displacement of the helix is equal to $AR{\cdot}p_h$ per rotation. When AR < 1, the helix picks up a volume of sand at each rotation. It can be assumed that particles must be small enough to enable this mechanism. The ratio of vertical displacement per rotation, to the maximum and average particle diameters is depicted in Fig. 5 (AR = 0.5 or 1.0) as a function of the scaling factor.

2.3. Contact model

The contact model used in this study is a modified Hertz-Mindlin relationship which is described in detail in the documentation of Itasca Consulting Group (2019) and O'Sullivan (2011). The normal stiffness is calculated automatically and is a function of the particle size. Therefore a single set of parameters can be used for all scaling factors and give similar results (Lommen et al., 2019). Particle rolling was inhibited to approximate the behaviour of angular sand grains with spherical particles. This technique was introduced by Ting et al., (1989) and later used to simulate boundary value problems (Arroyo et al., 2011; Sharif et al., 2020a). The contact model parameters are given in Table 5. The DEM particle parameters (G, ν, μ) were separately calibrated by Sharif et al. (2019) against triaxial tests undertaken on the sand material used in the centrifuge tests. Consequently, the validation of DEM simulations does not consist in tuning of the DEM parameters. The steel-soil interface friction coefficient was determined by direct shear tests

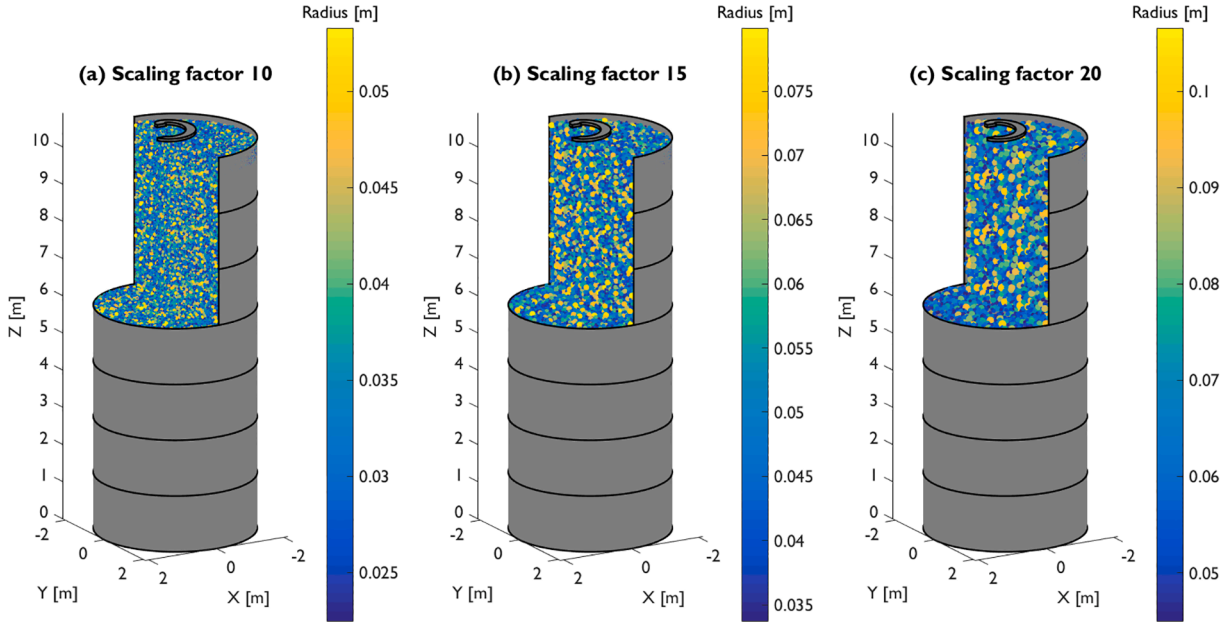

Fig. 3. Soil beds and servo-controlled cylinders used to imposed a constant stiffness at the boundary, the helix of the pile is depicted for scale comparison.

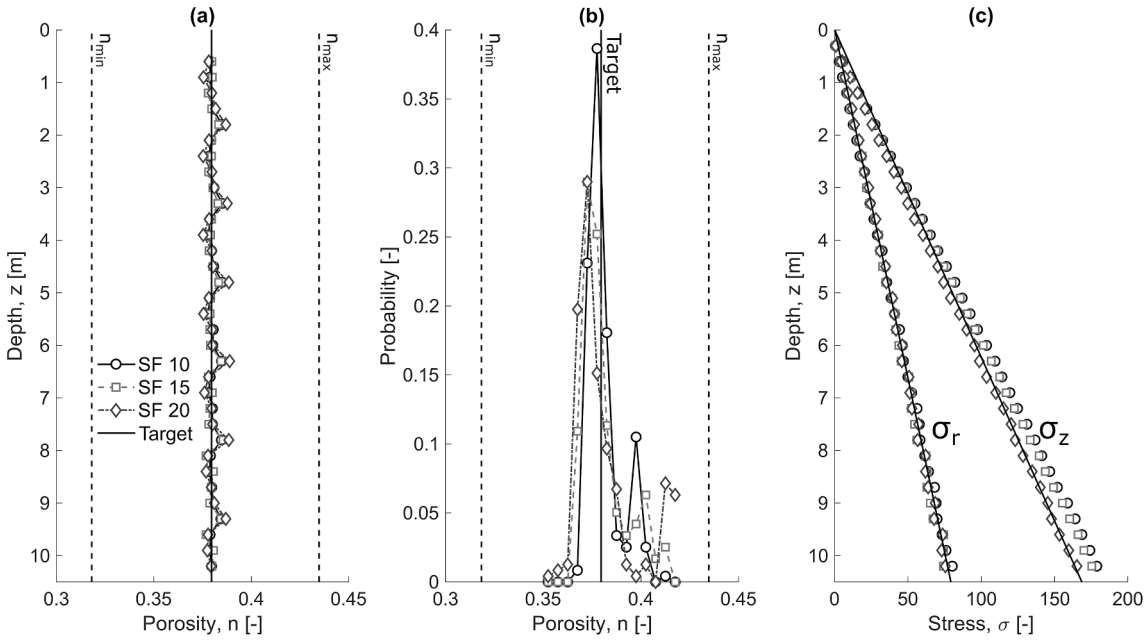

Fig. 4. Soil bed porosity distribution and initial stress state as a function of the particle scaling factor (SF), n_{min} and n_{max} and respectively the minimum and maximum porosities of the HST95 sand.

Table 4
Pile dimension to particle dimension ratios.

SF	D_s/d_{50}	$(p_h - t_h)/d_{100}$	$(D_h - D_s)/(2d_{50})$
10	7.8	2.74	3.63
15	5.2	1.82	2.42
20	3.9	1.37	1.81

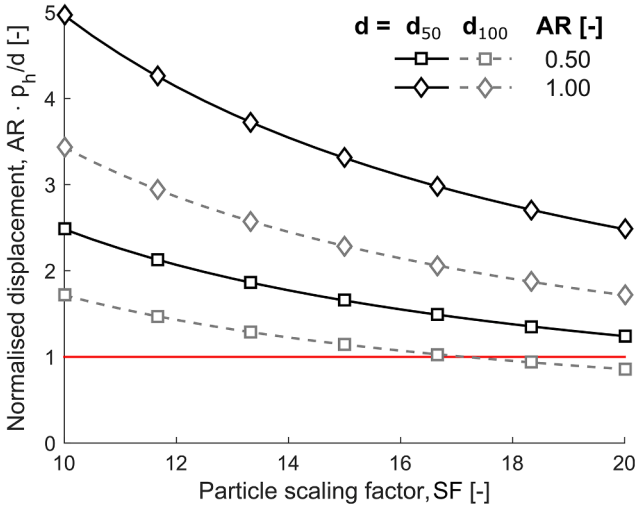

Fig. 5. Vertical displacement per helix rotation normalised by particle diameter (average d_{50} or maximum d_{100}) as a function of the particle scaling factor (SF) and advancement ratio (AR).

(Lauder et al., 2013) and was assumed to be identical to the particle-pile friction coefficient (μ_{pile}). The boundary walls (cylinders in Fig. 3) truncate the soil domain, therefore the particle–wall friction coefficient for these walls (μ_{wall}) is calculated based on the peak friction angle of the sand (~38.5°). The wall contact resolution was set to full (Itasca Consulting Group, 2019), with a cut-off angle equal to 20°. This ensures the contact continuity during the pile rotation for particles in contact with adjacent facets composing an approximate circular surface.

Table 5
DEM Contact model properties, contact model parameters from (Sharif et al., 2019).

DEM properties [unit]	Symbol	Value
Particle shear modulus [Gpa]	G	3
Particle Poison's ratio [-]	ν	0.3
Particle friction coefficient [-]	μ	0.264
Exponent stiffness	α_h	1.5
Shear-force scaling mode [-]	M_s	0
Damping ratio [-]	β	0
Dashpot mode [-]	M_d	0
Exponent dashpot	α_d	0
Pile interface friction coefficient [-]	μ_{pile}	0.445
Wall interface friction coefficient [-]	μ_{wall}	0.8

2.4. Installation procedure

Screw pile installation in the field is undertaken at a rotation rate ranging from 5 to 20 rotations per minute (Spagnoli et al., 2020) and can be assumed to be quasi-static. In the centrifuge tests, the rotation rate was equal to 3 rotations per minute. The DEM installation rate must be chosen as fast as possible to limit the computational cost and time of simulation, while maintaining quasi-static conditions. The inertial number (I) is often used as an indicator to determine whether a model behaves in a quasi-static manner. Da Cruz et al. (2005) proposed a definition of the inertial number based on the shear strain rate $\dot{\gamma}$, the density of the particles (ρ_s) and the confining pressure p_0'.

$$I = \dot{\gamma} d_{50} \sqrt{\frac{\rho_s}{p_0'}} \leq I_{max} \tag{3}$$

It is usually assumed that the inertial number must be maintained below a certain threshold (I_{max}), to ensure a quasi-static behaviour. However, the value of this threshold varies as a function of the authors or problem investigated, ranging from 0.001 (Da Cruz et al., 2005; Khoubani and Evans, 2018; Ciantia et al., 2019) to 0.01 (Janda and Ooi, 2016). The different terms of Equation (3) can be easily identified for

element testing modelling, such as plane shear or triaxial tests (e.g. Da Cruz et al. (2005) or Lopera Perez et al. (2016)) where the shear strain is relatively homogeneous. On the contrary, screw pile installation generates a more complicated shear strain regime due to the combination of helix and shaft rotation and penetration. In addition, the confining pressure ($p_0^{'}$) varies with depth and is influenced by the pile penetration itself. However, a simplified procedure is used to estimate the maximum penetration rate.

The vertical velocity of straight shafted piles (v_z) and the soil shear strain rate ($\dot{\gamma}$) can be related as follows (Ciantia et al., 2019):

$$v_z = \dot{\gamma} L_{pz} \tag{4}$$

where L_{pz} is a representative dimension of the plastic deformation zone associated with the vertical pile penetration mechanism, which has the order of magnitude of $3D_s$ in sand (Yang, 2006). An additional helix rotation-related mechanism was proposed by Sharif et al. (2020a) based upon theoretical developments. It assumes that the rotation rate of a screw pile (ω) and soil shear strain rate can be related as follows.

$$\omega = \frac{2\pi\dot{\gamma} L_{p\omega}}{D_h} \tag{5}$$

where $L_{p\omega}$ is a representative dimension of the plastic deformation zone associated with the rotation of the helix, equal to $4D_h$. However, the actual shape and dimensions of the penetration mechanism have not been investigated in detail. The pile rotation and penetration rates are dependent variables for a fixed AR

$$\omega = \frac{2\pi v_z}{ARp_h} \tag{6}$$

Therefore by combining Equations (3–6), it is possible to derive a criterion to estimate the maximum pile penetration rate ($v_{z,max}$) ensuring quasi-static conditions for both vertical penetration and rotation mechanisms.

$$v_{z,max} = \min(4p_h AR, 3D_c)\frac{I_{max}}{d_{50}}\sqrt{\frac{p_0^{'}}{\rho_s}} \tag{7}$$

The maximum penetration rate is a function of the initial confining pressure ($p_0^{'} = \sigma_v^{'}(1+2K_0)/3$) which is depth dependent. Therefore, one means of decreasing the CPU cost of the simulation is to increase the pile penetration (and rotation) rate as the helix penetrates the ground (Sharif et al., 2020a).

The inertial number that should be used to ensure quasi-static conditions is not well-defined, especially for boundary value problems and it was recently shown by Shire et al. (2021) that polydisperse materials might require slower loading rates to ensure true quasi-static conditions. A reference penetration rate ($v_{z,10}$) profile was calculated by using 0.01 as the maximum inertial number (I) and corresponds to AR = 0.5 and SF = 10 (Table 6). The maximum penetration rate profile is linear in AR, SF or I (Equation (7)). Therefore, the velocity profile corresponding to other conditions (AR, SF or I) can be calculated easily from Table 6. For instance, the penetration rate for AR = 1.0 is twice as fast while assuming a constant I.

The critical time step can be estimated by the following equation (Otsubo et al., 2017; Shire et al., 2021)

$$\Delta t_{crit} = 0.1\sqrt{\frac{m_{part}}{K_c}} \tag{8}$$

where m_{part} is the mass of the smallest particle and K_c is the stiffness of the contact between two of the smallest particles. The stiffness of the contact can be calculated as follows

$$K_c = \frac{G\sqrt{2R_{min}}}{1-\nu}\sqrt{\delta_{contact}} \tag{9}$$

where G and ν are the shear modulus and Poison's ratio of the particles and R_{min} is the smallest particle radius and $\delta_{contact}$ is the contact overlap between two particles, which can be assumed to be equal to 2% of the particle radius. Consequently, the time step is linearly increasing with the minimum particle radius size and then with the scaling factor applied to the PSD (see Table 7).

2.5. Summary of the simulations

Nine DEM simulations were undertaken (Table 8), in three soil beds with different particle SF (10, 15 and 20), for a total of 63 days of simulations. The pile velocity profile is characterised by the ratio (v/v_{ref}) between the imposed velocity and the reference velocity calculated based on Equation (7). This ratio was varied ($v/v_{ref} = 0.2, 1$ or 10) to investigate the inertial effects on the macroscopic behaviour of the pile. The smallest SF (10) could not be tested at a penetration rate slower than the reference one ($v/v_{ref} = 1$), as the simulation would have taken several months. Two advancement ratios were considered: overflighting (AR = 0.5) or pitch-matched (1.0), as centrifuge results at this ARs showed a clearly distinct behaviour. The installation between 0 and 1 m depth is the slowest part of the process, as the confining stress is low, whilst it does not have significant influence on deeper behaviour. Therefore, the velocity ratio (v/v_{ref}) was increased at the beginning (0–1m) of two simulations (1 and 3) which required the longest CPU time (see in Table 8).

2.6. Description of the centrifuge tests

Centrifuge tests were used to validate the DEM results and are described in detail by Cerfontaine et al., (2021), whilst the procedure is described in Davidson et al. (2020). Those tests were undertaken in medium-dense sand (average relative density 52%, porosity 0.38), prepared by dry pluviation. The dimensions of the prepared soil bed were 800x500x420mm and two installations tests were undertaken for each soil bed. A steel pile model whose geometry is identical to the one presented in section 2.1 was used. The pile models were installed at 50g, which corresponds to the DEM enhanced gravity field. Prescribed vertical and rotation rates were applied to the pile during installation while a load cell recorded the total vertical force and torque applied at the top of the pile. Three ARs of 0.25, 0.50 and 1.00 are compared with the DEM results in the following.

3. Results and discussion

The effect of numerical parameters (particle scaling factor and penetration rate) on the macroscopic behaviour (force and torque acting on the pile) are first identified, then interpreted based on micro-

Table 6
Pile vertical velocity as a function of depth for the reference case: SF = 10, I = 0.01, AR = 0.5.

Depth range [m]	$v_{z,10}$ [m/s]
0.0–0.5	0.076
0.5–1.0	0.108
1.0–2.0	0.152
2.0–3.0	0.216
3.0–5.0	0.264
5.0–8.0	0.342

Table 7
Constant time step as a function of the particle scaling factor (SF).

SF	Time step, Δt_{crit} [s]
10	$1.7{\cdot}10^{-7}$
15	$2.55{\cdot}10^{-7}$
20	$3.40{\cdot}10^{-7}$

Table 8
Summary of the simulations undertaken. † $v/v_{ref} = 10$ between 0 and 1 m depth. $^{\#}v/v_{ref} = 1$ between 0 and 1 m depth.

ID	SF [-]	v/v$_{ref}$ [-]	AR [-]	Duration [h]
1	10	1†	0.5	434
2	10	10	0.5	67
3	20	0.2$^{\#}$	0.5	345
4	20	1	0.5	91
5	20	10	0.5	11
6	10	1	1.0	251
7	20	1	1.0	47
8	15	1	0.5	170
9	15	1	1.0	89

mechanical observations.

3.1. Macroscopic behaviour

For each simulation, vertical force and torque acting on each subpart of the model can be calculated throughout the simulation. The particle to facet contact forces acting on each pile subpart can be easily identified. Therefore, the penetration resistance can be calculated by summing all vertical components of contact forces acting on a sub-part. The torque is calculated similarly by taking the cross product of the distance to the rotation axis and the contact forces associated with a sub-part. Results are then scaled up to prototype scale (velocity 1:1, distance 1:N, force 1:N^2 and torque 1:N^3, with N = 50) according to centrifuge scaling laws (Garnier et al., 2007). Force and torque evolution with depth were smoothed to identify the trends with depth.

3.1.1. Advancement ratio and particle scaling effect

Centrifuge tests presented by Cerfontaine et al. (2021) showed that overflighted (AR < 1) screw piles exhibited a reduction in crowd force necessary for their installation, which is consistent with previous DEM work (Sharif et al., 2020b). If the imposed AR is low enough, tension was generated in the pile. Three of those centrifuge tests (dashed lines) depict this behaviour in Fig. 6a. The vertical force (F_z) acting on the pile changes from compression (AR = 1.0) to tension (AR = 0.25), with AR = 0.5 generating almost no vertical force at all.

DEM simulations at two ARs (0.5 and 1.0) were undertaken for three scaling factors (SF = 10, 15 or 20) to explain this behaviour. All piles were installed at a same assumed inertial number ($I = 0.01$, see section 2.4). The DEM and centrifuge results are consistent and show a reduction in the vertical force (F_z) with a reduction of AR (Fig. 6a). The pitch-matched simulations (AR = 1.0) appear unaffected by the SF, while overflighted piles (AR = 0.5) experience a greater reduction in force as SF decreases. In comparison, the torque varies more for the pitch-matched than for the overflighted piles. The relative insensitivity of the AR = 1.0 simulations to SF, compared to simulations with AR = 0.5, suggests that two distinct penetration mechanisms take place as a function of AR. The identification of the overflighting (AR = 0.5) mechanism is one of the objectives of this paper and will be detailed in section 3.2.1. The penetration rate effect will be explained based on micro-mechanical observations in section 3.2.3.

The DEM enables a split of the pile base, shaft and helix penetration resistances. In all cases, the shaft penetration resistance is lower than 0.12MN and is not plotted here. Base (F_b) and helix (F_h) forces depicted in Fig. 7 are relatively insensitive to SF, if AR = 1.0. On the contrary (AR = 0.5), the helix component (Fig. 7a) is more in tension and the base component (Fig. 7b) is less in compression, as the SF is reduced.

Tsuha and Aoki (2010) assumed that the helix torque (T_h) is linearly proportional to the helix vertical force (F_h),

$$\frac{T_h}{F_h} = R_{eq}\tan(\psi + \delta) \tag{10}$$

where R_{eq} is an equivalent radius characterising the helix, ψ is the helix angle and δ the interface friction angle. However, forces (Fig. 7a) and torque (Fig. 8) associated with the helix do not seem to verify this model. When AR = 1.0, the torque increases with SF while the force is almost the same for all SF. When AR = 0.5, it is the opposite. Therefore, the ratio of helix torque to force is clearly not a constant as stated in Equation (10). This difference will be further explained in section 3.2.4.

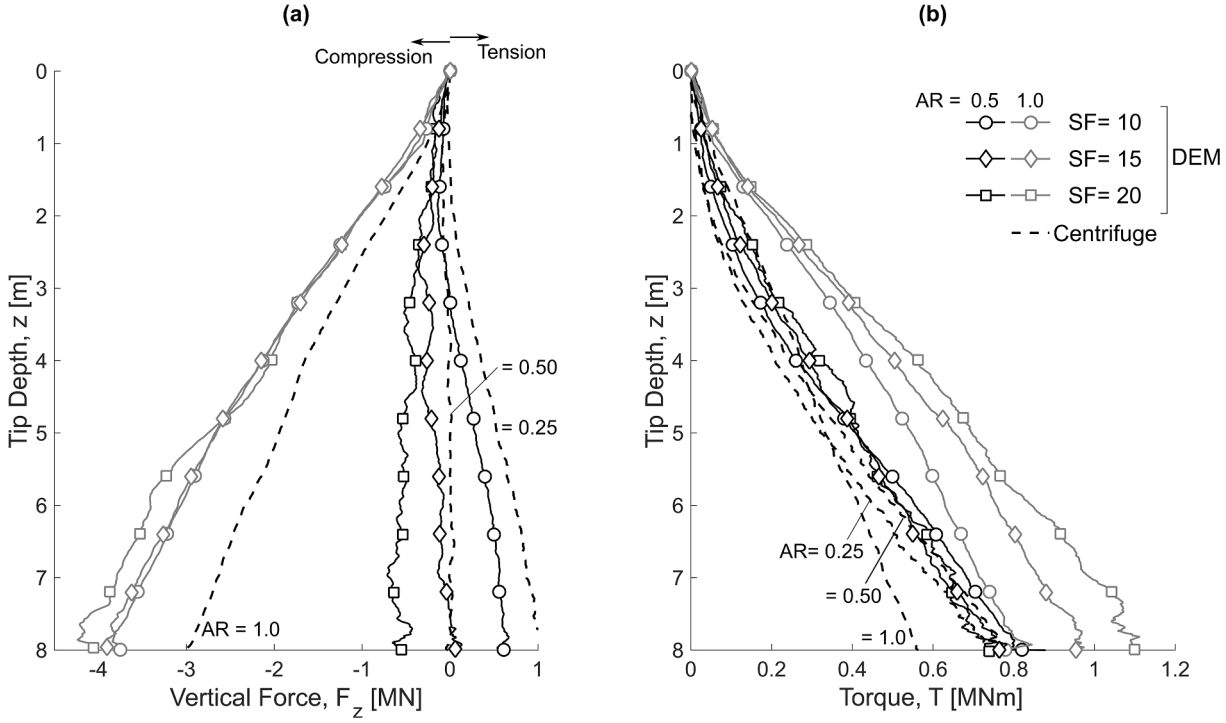

Fig. 6. Comparison between centrifuge (AR = 0.25, 0.5 or 1.0) and DEM (AR = 0.5, AR = 1.0) (a) measured vertical force and (b) torque, at the top of the pile as a function of the particle scaling factor (SF), $v/v_{ref} = 0.01$

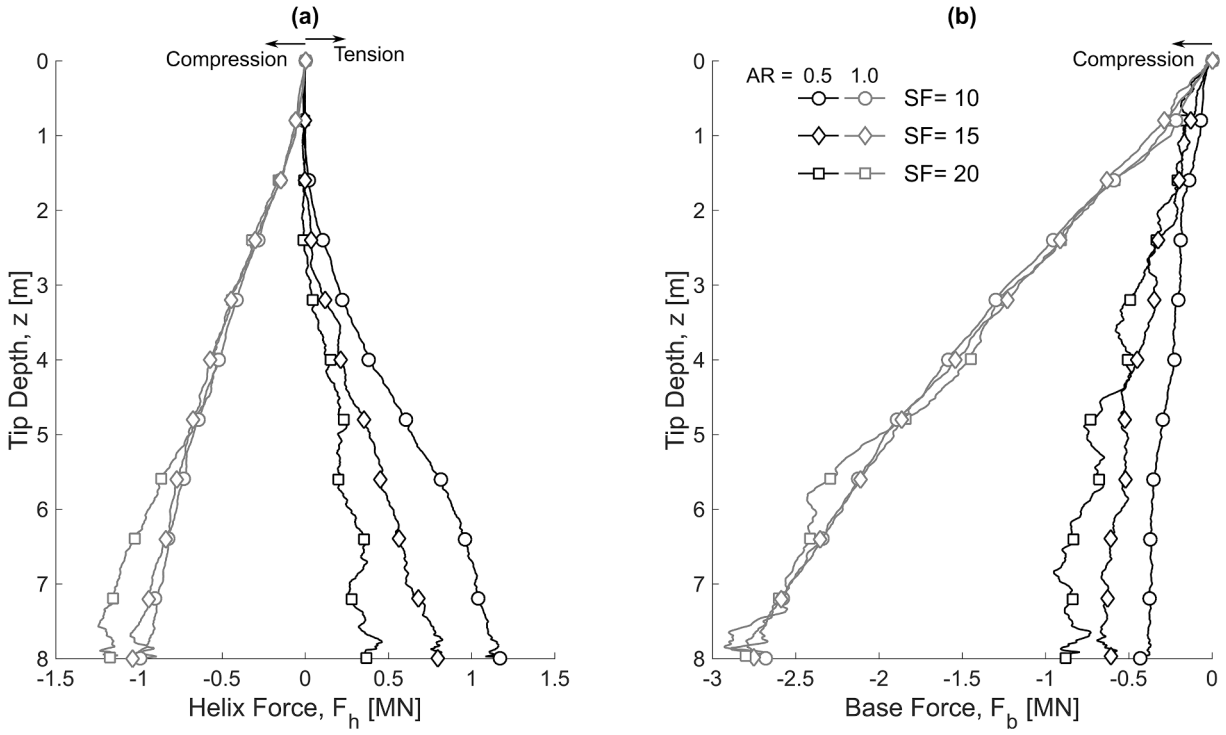

Fig. 7. Comparison between DEM (AR = 0.5, AR = 1.0) measured vertical force (a) acting on the helix and (b) on the base, as a function of the particle scaling factor (SF), $v/v_{ref} = 0.01$

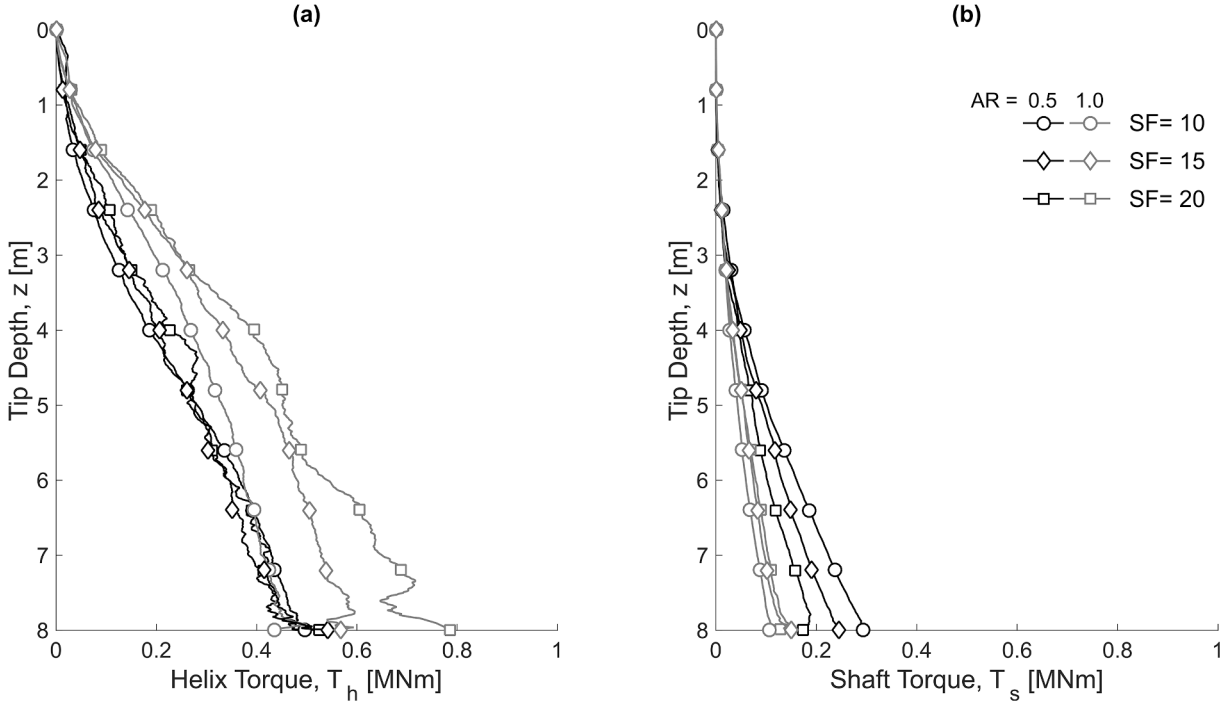

Fig. 8. Comparison between DEM (AR = 0.5, AR = 1.0) measured torque acting on the (a) helix and (b) on the shaft as a function of the particle scaling factor (SF),$v/v_{ref} = 0.01$

A second difference form this model (Equation (10)) is that there exist a case where the helix force tends to zero (SF = 20, AR = 0.5, Fig. 7a), while the torque remains constant (SF = 20, AR = 0.5, Fig. 8a). This can be explained by the fact that F_h is the difference of normal forces acting on both faces of the helix (upper $F_{h,u}$ and lower $F_{h,l}$), while T_h is the sum of contributions on both faces (upper $T_{h,u}$ and lower $T_{h,l}$). Therefore, if the upper and lower forces are equal in magnitude, the resultant F_h is equal to zero, while the torque is not. If the helix is clearly in compression ($F_{h,l} \gg F_{h,u}$) or clearly in tension ($F_{h,u} \gg F_{h,l}$), Equation (10) is verified. Otherwise, the torque is underestimated.

Fig. 8a shows that the helix torque contribution of overflighted piles (both ARs, all SF) increases almost linearly with depth. The shaft

contribution (Fig. 8b) is more non-linear than the helix and more non-linear for AR = 0.5 than for AR = 1.0. Reducing the SF (AR = 1.0 in Fig. 8a) reduces the helix torque, which is probably due to the cutting edge penetration resistance (see section 3.2.4). On the contrary, reducing the SF (AR = 0.5, Fig. 8b) increases the shaft torque, which is due to helix shaft interaction (see section 3.2.1).

In the absence of instrumented pile models in the centrifuge, it is not possible to compare the DEM helix or shaft contribution with experimental results. However, smaller particles will give more accurate results, by enabling a more accurate description of the physical mechanisms and will also reduce the noise in the results as observed by Khosravi et al., (2020).

3.1.2. Penetration rate

The penetration rate (v/v_{ref}) was varied to simulate the overflighting installation (AR = 0.5 only) of the pile, for two SF (10 or 20). Fig. 9a shows that only one simulation (SF = 10, v/v_{ref} = 1) creates some tension in the pile. There is no clear effect of the penetration rate in the SF = 20 results, the maximum total force being obtained for v/v_{ref} = 0.2 and the minimum for v/v_{ref} = 1. There is less variation in the total torque result (Fig. 9b).

By splitting the helix and base penetration resistances, Fig. 10 shows that the penetration rate affects the pile response in all cases, but those effects balance each other. Fig. 10a shows that the helix generates some pull-in in almost all cases (SF = 10 and 20, $v/v_{ref} < 10$) due to the overflighting effect. The magnitude of the pull-in force increases with a reduction in penetration rate (Fig. 10a, both SF). For SF = 20, there is little change from v/v_{ref} = 1 to 0.2, but the pull-in force almost doubles from SF = 20 to 10 (v/v_{ref} = 1). The base force seems to have a different trend as a function of the SF, it increases (SF = 20) or is reduced (SF = 10) in magnitude with a reduction in penetration rate. This opposite trend is due to the complex superposition of SF and penetration rate influences. The fastest penetration rate creates too much inertial effect, as will be further demonstrated (section 3.2.3) and is not representative of real conditions.

3.2. Microscopic interpretation

DEM modelling is similar to a highly instrumented experiment, as contact forces between particles and their exact positions are directly available. Microscopic interpretation can be used to understand the macroscopic behaviour observed in section 3.1, and especially the overflighting mechanism (AR = 0.5), and the influence of SF and penetration rate. Ultimately, microscopic information can be used to reassess hypotheses made to estimate the penetration rate (section 2.4).

3.2.1. Overflighting (AR = 0.5) installation mechanism

The simulation with the smallest SF (10) and slowest penetration rate was selected as a reference, because it is the closest to the real particle scale and installation rate conditions. To identify the installation mechanism, four snapshots of particle displacements (Δ_x, Δ_y and Δ_z) and contact forces were taken. They correspond to 4 rotations of 10°, 20°, 65° and 360° from a pile initially embedded at 7 m depth. The vertical displacement (Δ_z), horizontal displacement ($\Delta_h = \sqrt{\Delta_x^2 + \Delta_y^2}$) and force chains are represented in Fig. 11, Fig. 12 and Fig. 13 respectively. In these figures, only particles/contacts above and below the helix are represented for clarity, although the sand bed extends beyond the helix dimensions.

Fig. 11a-b shows that a small rotation induces an upwards movement of particles in front of the helix cutting edge, whilst fewer particles move beneath the helix. After 65° rotation (Fig. 11c), particles close to the helix upper face are moved upwards, whilst particles that lost contact with the helix due to its rotation experience a displacement downwards. At the end of one full rotation (Fig. 11d), most particles just above the helix have been moved upwards by more than 0.05 m. In addition, a zoom on the helix (not represented) shows that a gap exists between particles and the lower face of the helix. Fig. 12a-b show that a small rotation induces greater horizontal than vertical displacement, as the helix cutting edge pushes particles. This helix penetration induced displacement happens also for pitch-matched installation. Fig. 12c shows that some horizontal displacement also occurs further away from

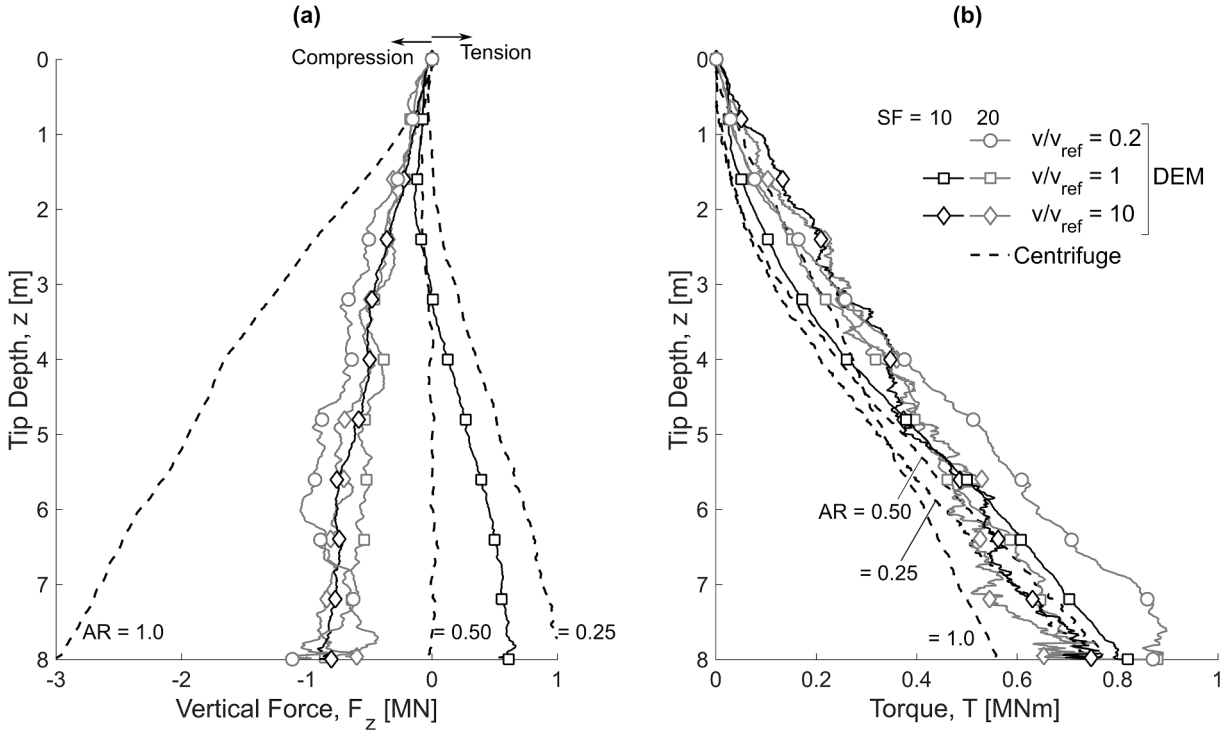

Fig. 9. Comparison between centrifuge (AR = 0.25, 0.5 or 1.0) and DEM (AR = 0.5) (a) measured vertical force and (b) torque at the top of the pile as a function of the installation velocity (v/v_{ref}) and particle scaling factor (SF).

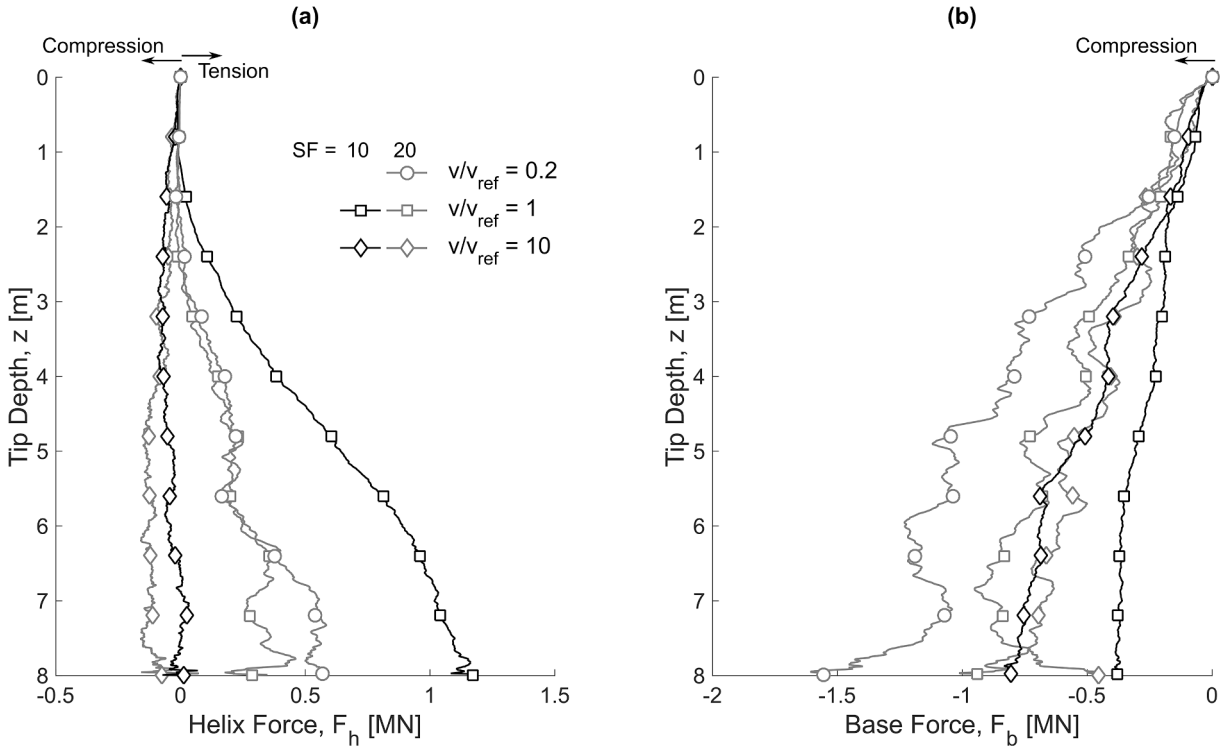

Fig. 10. Comparison of (a) helix and (b) base vertical forces measured in DEM simulations as a function of the installation velocity (v/v_{ref}) and particle scaling factor (SF).

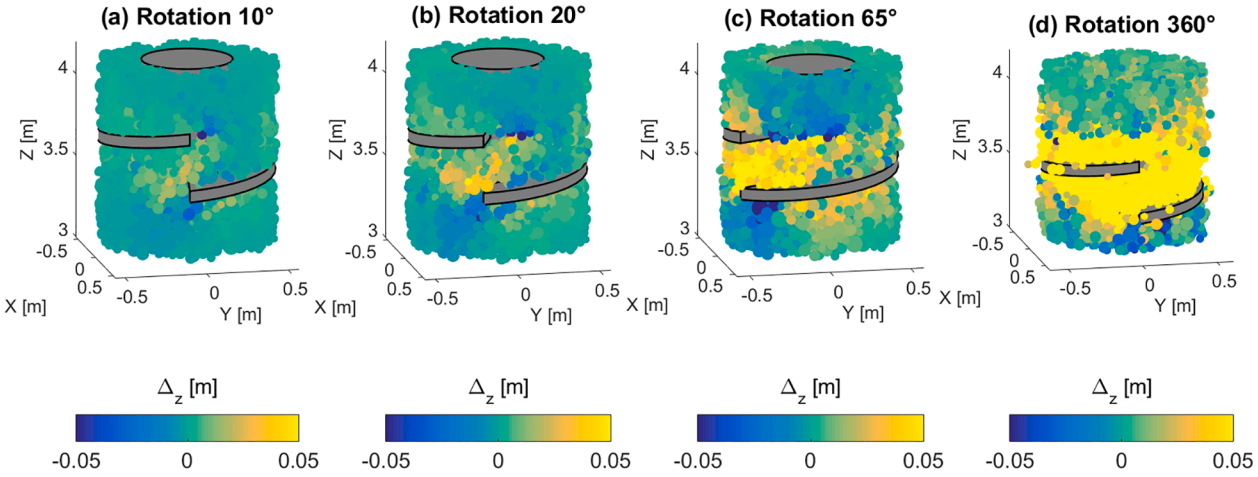

Fig. 11. Vertical displacement of particles during a 360°helix rotation, starting at 7 m depth (SF = 10, v/v_{ref} = 1, AR = 0.5). Displacement is capped to [-0.05 m, 0.05 m].

the cutting edge along the helix upper face. After a full rotation (Fig. 12d), most particles above the helix have been affected by some horizontal displacement, which could be in the radial and/or orthoradial direction. Fig. 13a-d are all similar. Contact forces on the helix upper face are low close to the cutting edge, but increase in magnitude along the helix, to be maximum close to the upper edge. Contact forces have a great magnitude on the cutting edge, while it is low under the helix, which is consistent with the formation of a gap.

A theoretical model is presented in Fig. 14 to summarise the different observations and explain the macroscopic pile behaviour. The cutting edge of the helix penetrates the soil due to its rotation and creates a passive wedge (Fig. 14d). This forces particles to move above or beneath the helix. In this case, the overflighting movement seems to move more particles above the helix. Once particles have been picked up by the helix, and are in contact with its upper face, they are forced to move upwards due to the oveflighting movement (introduced in Fig. 1). Theoretically, a particle initially in contact with the cutting edge that could only move vertically would be subjected to a vertical displacement (Δ_z) that varies with the rotation of the helix ($0 \leq \theta \leq 2\pi$).

$$\Delta_z = (1 - AR) \cdot p_h \cdot \frac{\theta}{2\pi} \leq (1 - AR) \cdot p_h \tag{11}$$

However, the surrounding soil opposes the imposed vertical movement of particles and acts like a non-linear spring progressively compressed (Fig. 14a), which increases the vertical stress acting on the helix (σ_v). This normal force acting downwards on the upper face of the helix creates the pull-in force acting on the pile. As a corollary effect, the radial stress (σ_r) acting on the shaft in the vicinity of the helix will be

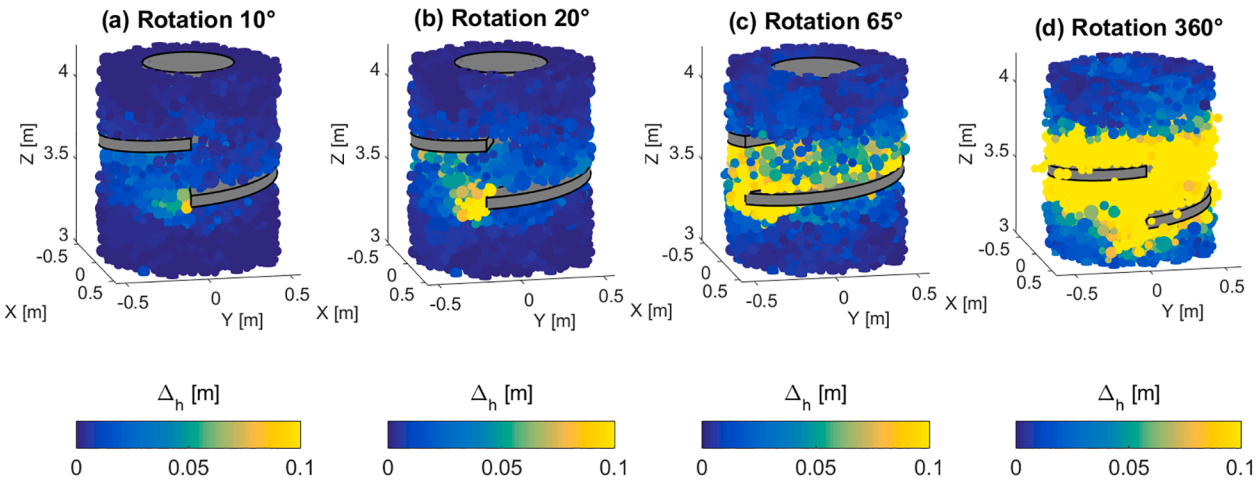

Fig. 12. Horizontal displacement of particles during a 360°helix rotation, starting at 7 m depth (SF = 10, v/v_{ref} = 1, AR = 0.5). Displacement is capped to [0 m, 0.1 m].

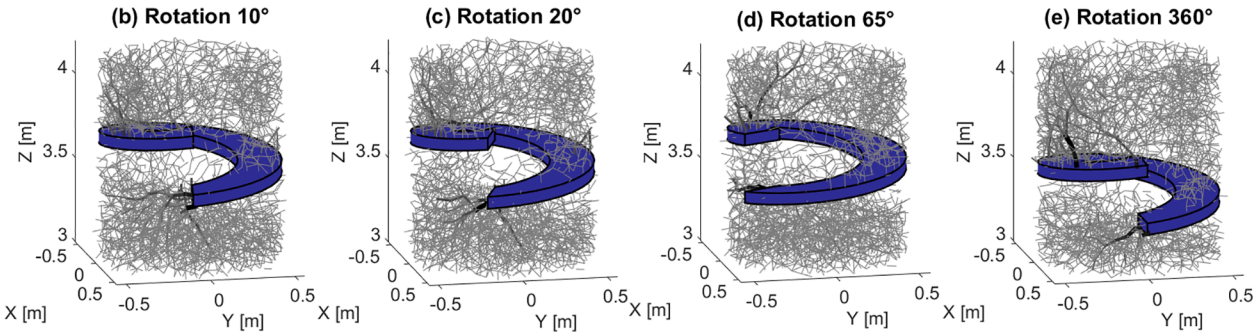

Fig. 13. Force chains during a 360°helix rotation, starting at 7 m depth (SF = 10, v/v_{ref} = 1, AR = 0.5).

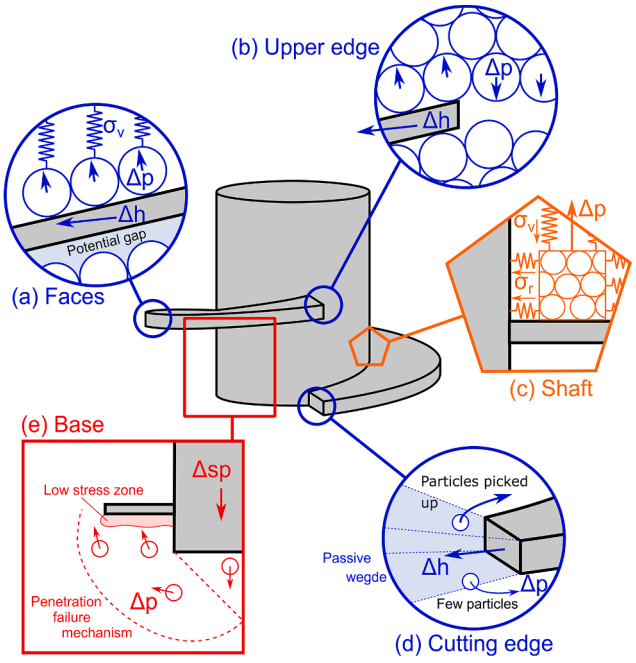

Fig. 14. Summary of the overflighting mechanisms created by the helix penetration, Δh is helix displacement, Δp is particle displacement and Δsp is the screw pile displacement.

increased by the squeezing of particles (Fig. 14c), which will increase the torque resistance. Finally, particles that were close to the helix upper edge tend to fall down (Fig. 14b) after the helix has rotated.

The overflighting movement of the helix has the potential to create a gap under the helix (Fig. 14a), simply because the helix moves more laterally than vertically. The existence of this gap depends on the degree of overflighting, but also on the particles displaced laterally by the pile base penetration (Fig. 14e). The base penetration resistance depends on the interaction between the pile base failure mechanism and the helix (Fig. 14e), and could be idealised by a classical bearing capacity equation in cohesionless soils

$$\frac{4F_b}{\pi D_s^2} = qN_q + \frac{1}{2}\gamma_{soil} D_s N_\gamma \tag{12}$$

where q is the surcharge term, γ is the soil unit weight, and N_q and N_γ are bearing factors. If the pile is overflighted, with the AR lower than a critical value, there is a gap or a very low stress distribution under the helix. In this case, the surcharge term (q) tends to zero. Otherwise, particles displaced by the helix tend to close this gap and the helix is under compression. In this case, the surcharge term tends to 'confine' the base failure mechanism and to increase the penetration resistance. This is what happens for the pitch-matched installation (AR = 1.0) with both base and helix in compression. In this case, the penetration mechanism also changes to some more classical flow around (the helix) mechanism similar to pile jacking installation (White and Bolton, 2004).

3.2.2. Estimation of strain rate

Velocity and shear strain rate profiles are calculated in this section to give further insight into the failure mechanism (AR = 0.5) and to

evaluate the hypotheses made in section 2.4. A snapshot of particle velocities was taken when the pile reached 8 m embedment (SF = 10, $v/v_{ref} = 1$). Particle velocity was averaged by using measuring boxes. Twelve angular sectors (30° opening) were defined, starting from the cutting edge, as shown in Fig. 15d. Each sector is located above the helix plate. Each sector was further subdivided radially (0.15 m ≈ $2d_{50}$) and the average velocity of all particles enclosed in this subdivision was calculated.

Radial (positive outwards), orthoradial (positive in the direction of the helix rotation) and vertical (positive upwards) velocities are depicted in Fig. 15a-c and depict some inhomogeneity along the helix. Along the lower helix part (0-150°), the orthoradial (Fig. 15b) and vertical (Fig. 15c) velocities are positive, indicating upwards movement of particles, pushed by the helix. Along the upper part of the helix (150°-360°), both vertical and orthoradial velocities change sign, indicating particles sliding along the helix. This is due to the progressive squeezing of particles (Fig. 14e) and creates generally positive radial velocities (Fig. 15a)

An approximation of the shear strain rate was obtained by calculating the gradient of orthoradial and vertical velocities in the radial direction (Fig. 15e-f). For both strain rates, the maximum values generally occur close to the edge of the helix. Fig. 15 shows that the orthoradial shear strain decreases rapidly with radial distance. For instance, at a distance of 1.1 m ($1D_h$) from the pile axis, the orthoradial shear strain has dropped below 0.05 s^{-1}, while the maximum value was 1.5 s^{-1} close to the helix. Equation (7) assumed that the plastic shear zone extended to $4D_h$ radially and the calculated maximum shear strain rate should be approximately 0.5 s^{-1}. Fig. 15 suggests that Equation (7) should be amended to include vertical and orthoradial shear strain rates, but also a reduced plasticity zone dimensions (radius ~ $3D_h/4$ from pile axis of rotation).

3.2.3. *Penetration rate effects*

The main hypothesis of the determination of the pile penetration rate (Equation (7)) and in the field is the soil quasi-static behaviour. This can be evaluated by calculating the average mechanical ratio (η) which represents the average out of balance forces in the sand bed, namely normalised inertial forces, and could be compared to the inertial numbers ($I = 0.002, 0.01$ or 0.1) which implicitly correspond to the penetration rates used in section 3.1.2. Fig. 16 shows that the mechanical ratio (Fig. 16a) is well correlated with the imposed velocity profile (Fig. 16b).

Fig. 16a shows the inertial number as used in Equation (3) is a good proxy for η, as they are well correlated and have the same order of magnitude. However, Equations (3–7) postulated that η would remain constant with depth because increasing confining stress should reduce inertial effects. Fig. 16a shows that this is not the case and this hypothesis is not completely valid.

Contrary to element test simulations, screw pile penetration generates highly non-homogeneous effects and a global value (η) may hide local effects. A particle mechanical ratio (η_p) is introduced and represents the relative magnitude of inertial forces with respect to the stabilising forces, at the scale of each particle. The ratio (η_p) is calculated as the norm of the resulting contact ($\boldsymbol{F}_c$) and gravity ($\boldsymbol{G}_p$) forces acting on a particle, divided by the sum of the norm of all forces

$$\eta_p = \frac{\| \sum \boldsymbol{F}_c + \boldsymbol{G}_p \|}{\sum \|\boldsymbol{F}_c\| + \|\boldsymbol{G}_p\|} \tag{13}$$

A value of η_p close to zero indicates quasi-static conditions, whilst values close to one indicate an unstable particle or a particle in free fall. This ratio can be directly compared with the inertial number at the scale of one particle, also defined as the ratio of inertial to confining forces (Shire et al., 2021).

Fig. 17 depicts the inertial ratio for each particle (η_p), at the end of the installation (depth = 8 m) for SF = 10 or 20 and three installation rates. This figure shows that inertial forces increase in proportion ($\eta_p \rightarrow 1$) as the pile penetration rate increases. In addition, they are not homogeneously distributed. High η_p particles are mostly located above

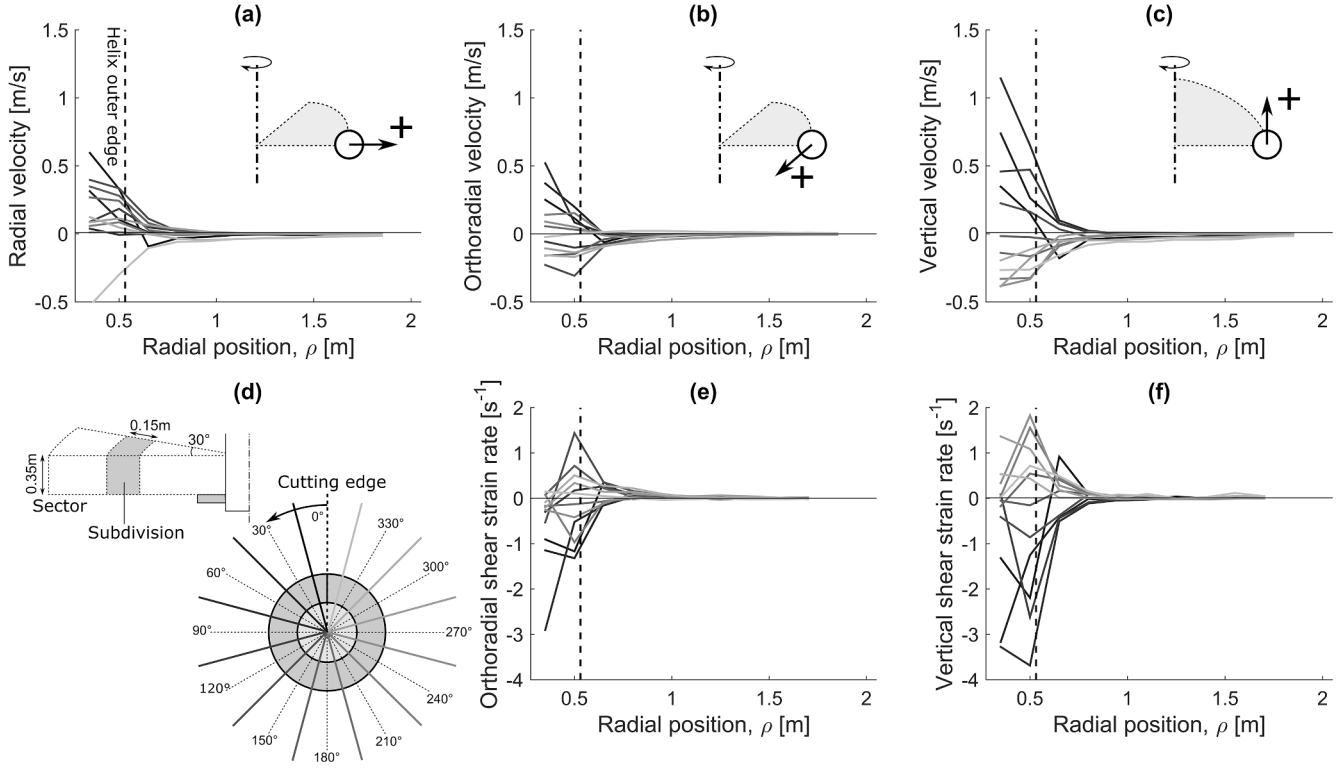

Fig. 15. Radial (a), orthoradial (in horizontal plane)(b) and vertical (c) velocities; in the orthoradial (f) vertical shear strain; Snapshot of simulation SF = 10, $v/v_{ref} = 1$, AR = 0.5 at 8 m embedment depth.

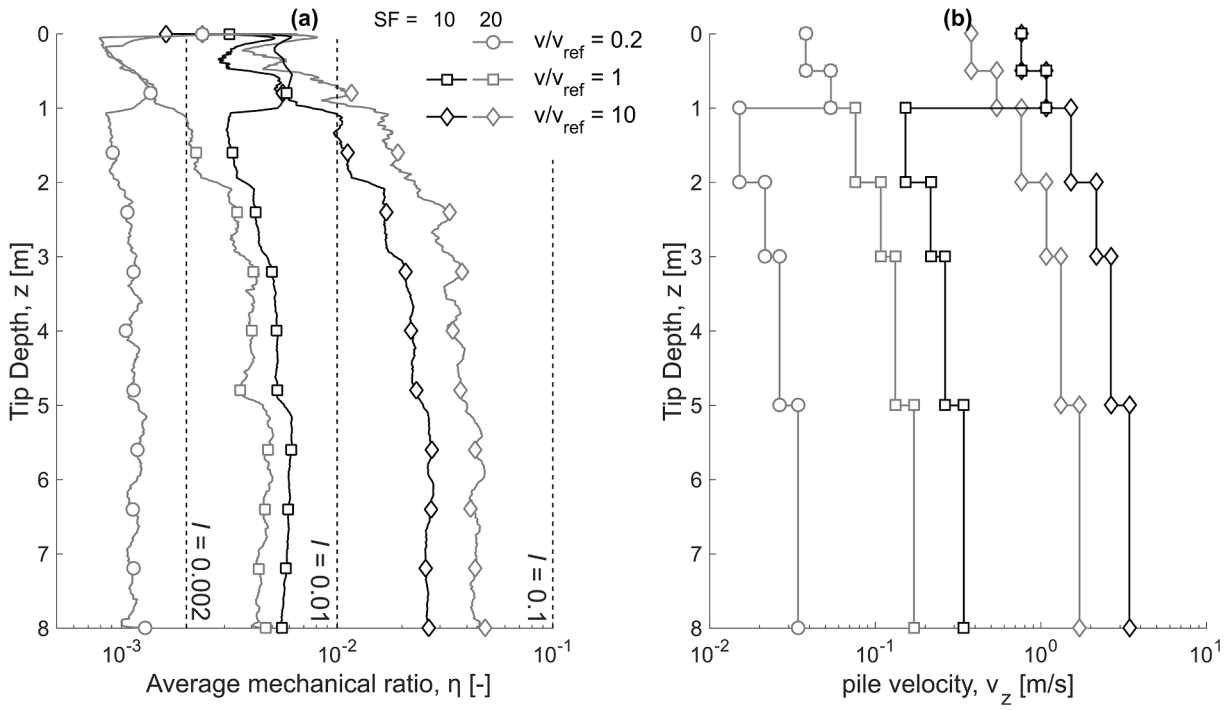

Fig. 16. Comparison of (a) the average mechanical ratio as a function of the installation velocity and particle scaling factor; (b) imposed pile velocity with depth.

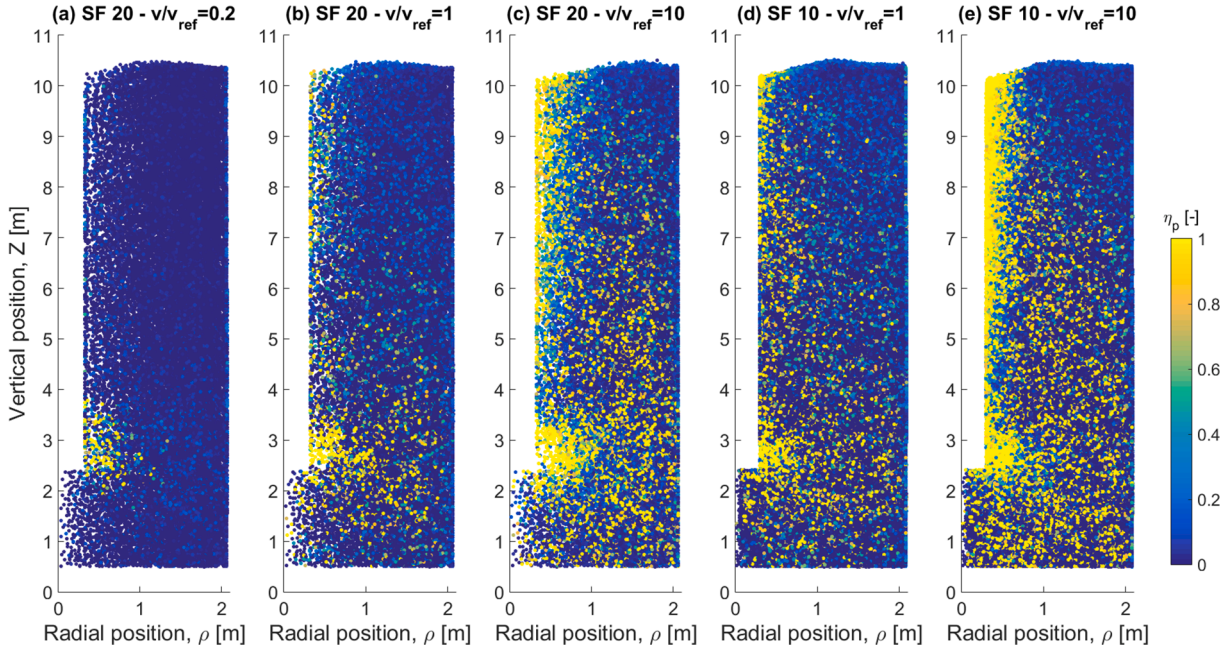

Fig. 17. Inertial ratio of the individual particles (represented with the same radius) as a function of the installation velocity (v/v_{ref}) and particle scaling factor (SF).

the helix at the slowest rate ($v/v_{ref} = 0.2$, Fig. 17a), which is consistent with particles being displaced by the helix cutting edge (Fig. 14d) or "falling off" the upper edge (Fig. 14b). When the penetration rate increases ($v/v_{ref} = 1.0$), more high η_p particles appear around the helix and close to the shaft, especially at shallow depth (z = 7–10 m, Fig. 17b and d). Unstable particles are everywhere at the faster installation rate ($v/v_{ref} = 10$, Fig. 17 c and e). This non-homogeneity is not accounted for in Equation (7).

Higher penetration rates are associated with reduced base penetration resistance and helix pull-in (SF = 20) in section 3.1.2. Particles with high η_p are less stable and less likely to contribute to force chains, hence a reduced penetration resistance and pull-in.

3.2.4. *Particle scale effects*

Fig. 18 depicts a zoom of particles total velocity ($v_{tot} = \sqrt{v_x^2 + v_y^2 + v_z^2}$) around the helix for the three slowest penetration rates depicted in section 3.2.3. In all cases, an empty volume (framed in Fig. 18) is created by the rotation of the helix upper edge. The faster the rotation rate, the greater this volume will be, as particles need some time to 'fall'. The maximum particle velocity occurs just in front of the cutting edge at the lowest SF (Fig. 18a) and is consistent with the helix linear

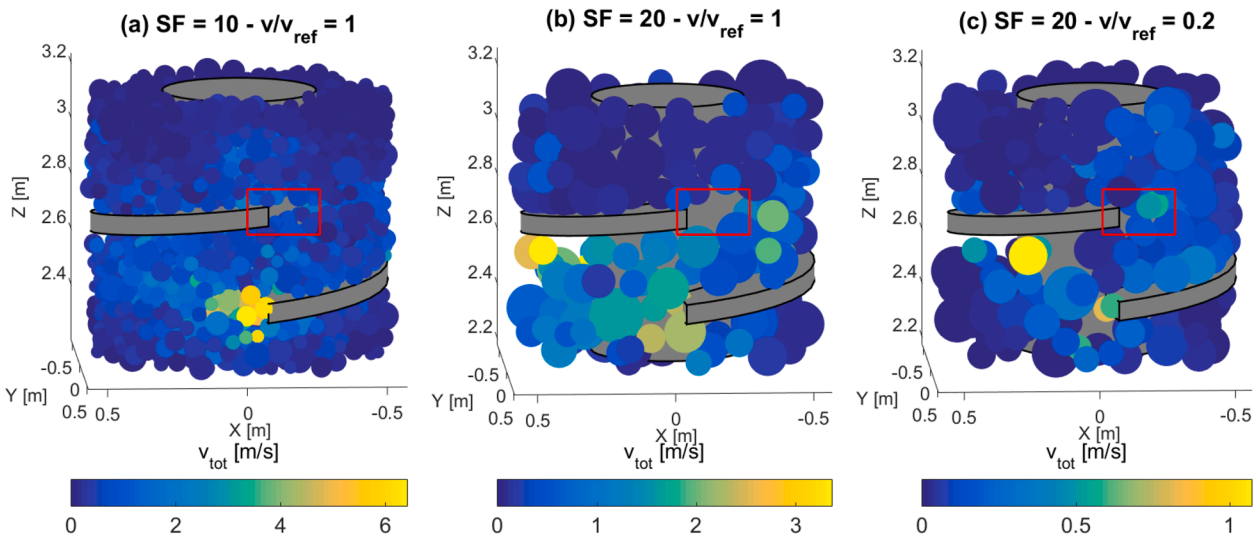

Fig. 18. Comparison of the particle total velocity around the helix (H = 8 m, AR = 0.5) for two different particle scaling factors and installation velocity $v/v_{ref} = 1$. Only particles close to the helix are shown.

velocity ($= \omega D_h/2$). In the other two subfigures (Fig. 18b-c), the highest particle velocity happens further away. It is believed that large particles impede the normal development of the passive wedge and cutting edge penetration mechanism. Consequently, larger particles (SF = 20) are pushed away in front of the cutting edge, whilst the smaller particles (SF = 10) are "picked-up" more easily. This process seems to be more prone to creating dynamic effects, as particles (SF = 20) seem to 'fly' in front of the cutting edge. This will create a looser soil state, which is more compressible and ultimately will reduce the pull-in force created, as observed in 3.1.1. This can be observed in Fig. 19, where all particle-helix contacts have been plotted in plan view. There are many more contacts acting downwards on the helix upper face (square markers) than acting upwards on the lower face (circular markers), which again explains the helix pull-in. The low number of circular markers indicates that there are almost no particle-helix contacts underneath the helix, hence potential for gapping (as per Fig. 14a).

The helix penetration is an inherently dynamic process and particles are forcibly moved upwards by the cutting edge. Slowing down the penetration rate gives more time for the 'picked up' particles to come back into contact with the helix. This is demonstrated by comparing Fig. 19b and c, where the density of contacts just above the cutting edge is higher at the slowest penetration rate.

As a corollary effect, it can be concluded that the overflighting mechanism will be more efficient in fine (e.g. sand) than coarse (e.g. gravel) granular soils. The cutting edge penetration mechanism will pick up fine particles more easily. In addition, there exists a low AR at which no additional particles can be picked up, because their dimensions (average particle diameter, d_{50}) becomes too large with respect to the helix vertical displacement per rotation ($AR{\cdot}p_h$). In this case, particles will simply be pushed by the helix cutting edge and not be picked up. This means that no additional pull-in can be mobilised to compensate for the pile penetration resistance, which is termed 'refusal'. Refusal can happen for a high AR in coarser material in the field, or with higher SF in DEM simulations.

The model of Tsuha and Aoki (2010) (Equation (10)) does not include the contribution of the cutting edge to the total torque, whilst it

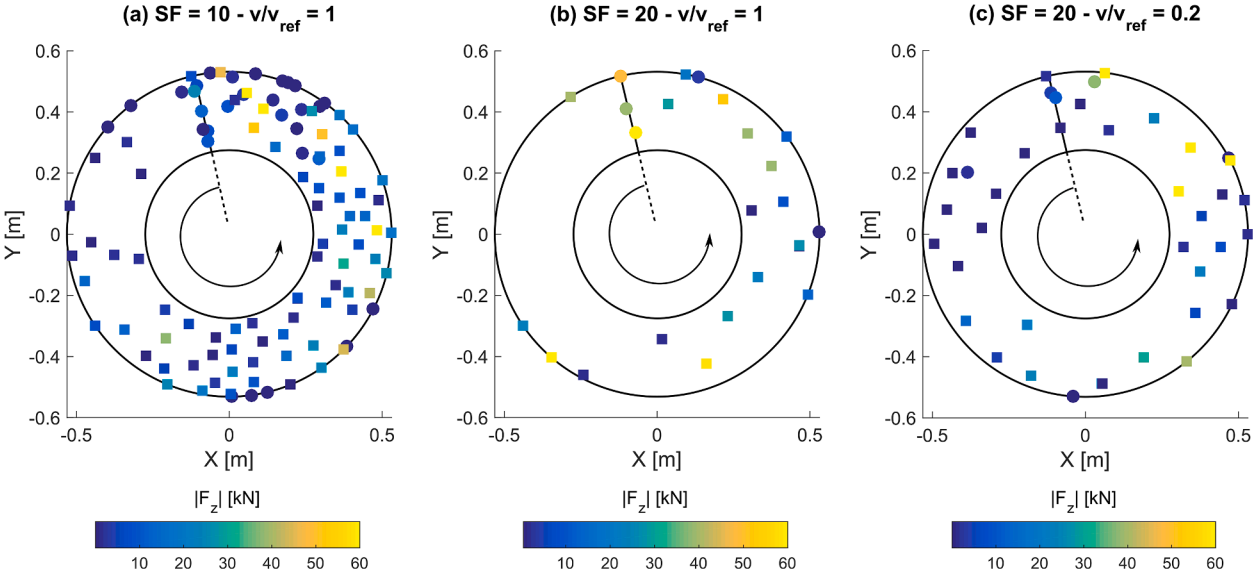

Fig. 19. Comparison of the contact forces along the helix as a function of the particle scaling factor (SF). Square markers denote forces oriented downwards on the helix upper face, circular markers oriented upwards on the helix lower face. The colour bar is capped at 60kN. The arrow indicates the helix direction, from lower to upper edge, AR = 0.5.

is included by other researchers (Davidson et al., 2020), although it is difficult to quantify its contribution experimentally. The cross product of each helix contact force ($F_{h,c}$) with its position vectors gives the contribution to the helix torque ($T_{h,c}$). Each combination ($F_{h,c}$,$T_{h,c}$) was plotted in Fig. 20 (SF = 10, 15 or 20, 8 m embedment depth), and markers were coloured as a function of the contact vertical position (0 m = cutting edge lower point). Fig. 20 clearly shows that there exists a linear relationship, verifying Equation (10), between some (but not all) of the forces and torques corresponding to contacts on both faces of the helix. The other datapoints belong to the helix cutting edge and exhibit greater torque contributions whose total ($T_{h,c-e}$) increases with the SF. This contribution ranges in proportion from 30% (SF = 10) to 70% (SF = 20) of the total helix torque. This explains why the measured helix force (F_h) was increasing in Fig. 7 with a reduction in SF, while the helix torque (T_h) remained constant. An increase in torque from the helix faces was compensated for by a reduction in the cutting edge contribution. A similar conclusion could be drawn for the pitch-matched installation. From a practical point of view, greater torque can be expected during the installation of screw piles in coarser materials e.g. gravels than in sands.

4. Conclusion

This work presents DEM simulations of screw pile installation in sand. The goal of the paper was to identify the penetration mechanism associated with a low advancement ratio (AR < 1) and investigate how numerical parameters, such as pile penetration rate or particle scaling factor (SF) affect the results. Three soil beds were created with an enhanced gravity identical to centrifuge tests. They were all composed of the same HST95 sand, whose particle scaling distribution was multiplied by a SF (=10, 15, 20). The boundaries of the problem were truncated and replaced by a constant stiffness servo-control, to limit the computational cost of the simulation. A screw pile model was installed at two different advancement ratios (AR = 0.5), simulating overflighted and pitch-matched (AR = 1.0) installations.

Several mechanisms occur simultaneously during the installation. The DEM enables their identification, which can inform the analysis of experimental results or field tests. The cutting edge penetrates the ground and creates a passive wedge. The rotating helix picks up particles, and the rotation progressively elevates and "squeezes" the ground, which in turns generates some pull-in effect (pile in tension), observed in the DEM and centrifuge tests. The penetration of both the pile base and helix cutting edge were shown to require a greater force in coarser soil beds which is analogous with moving into coarser material e.g. gravel.

All simulations exhibited a reduction in the vertical force with AR varying from 1.0 to 0.5, with smaller particles (SF = 10) enhancing the creation of pull-in along the helix and reducing the base penetration resistance. The smallest tested scaling factor (SF = 10) led to the most satisfactory approximate of the centrifuge overflighted tests (AR = 0.5). Scaling of the particles must be assessed with respect to the most relevant mechanisms: the helix cutting edge penetration and reduced displacement of the helix per rotation. This study also demonstrated that screw anchors can be installed in coarser materials, such as gravel, although at the cost of greater crowd force or torque during installation.

The pile penetration rate (linearly proportional to the inertial number) was varied (from 0.002 to 0.1) and inertial effects were locally identified close to the helix even at the slowest penetration rate. An inertial number equal to 0.01 was also shown to be an upper limit to reproduce the correct installation mechanism. It is advised to reduce this value if the simulation time remains acceptable, although the influence on the final results was shown to be smaller than the SF effect. The *a priori* assessment of the inertial effects should be improved by taking local effects, such as cutting edge penetration mechanism or shearing in multiple directions, into account.

Further work is necessary to investigate whether the combination of smaller particle and slower penetration rate could improve the DEM prediction. However, the number of particles and smaller time step that would be necessary make this simulation cumbersome. New experiments can also be undertaken to assess the pile installation rate/scaling effects or monitor more closely the split between helix/shaft/base penetration resistances.

CRediT authorship contribution statement

B. Cerfontaine: Conceptualization, Methodology, Software, Formal

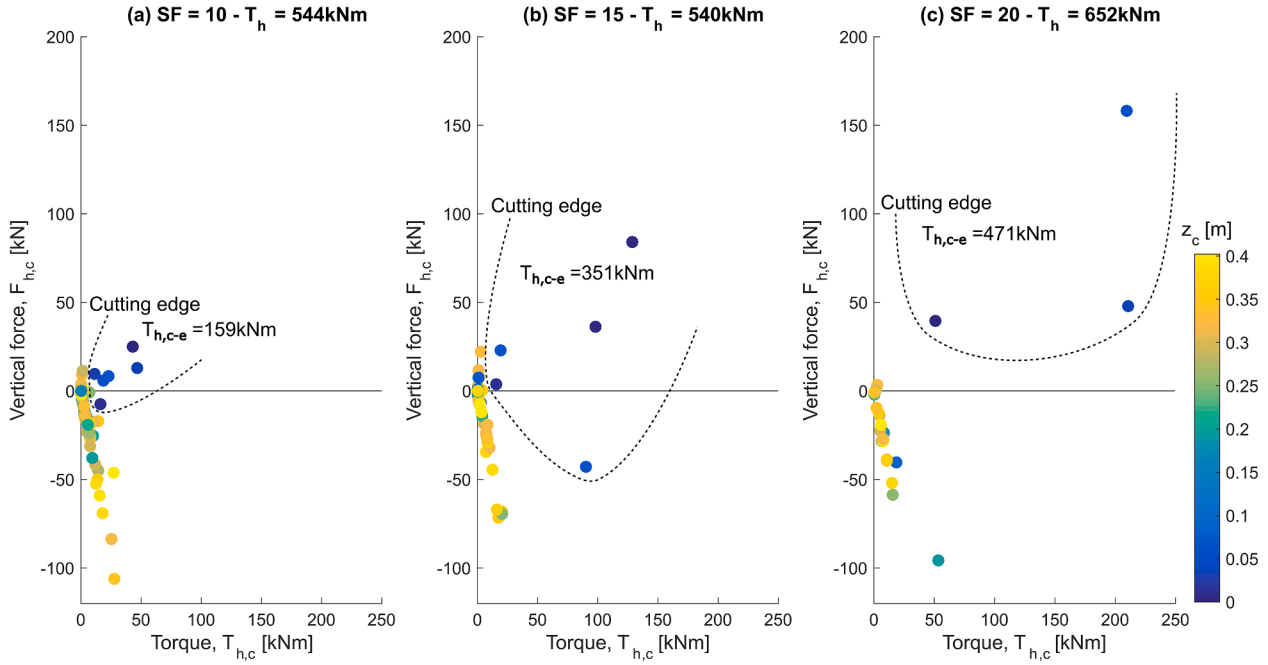

Fig. 20. Comparison of the torque ($T_{h,c}$) and force ($F_{h,c}$) contributions of each contact force acting on the helix, as a function of the scaling factor (SF), AR = 0.5, z = 8 m. The colour indicates the position of contact, between zero (cutting edge of the helix) and 0.4m (upper edge). The dotted line identifies the points belonging to the cutting edge.

analysis, Writing – original draft. **M. Ciantia:** Funding acquisition, Writing - review & editing. **M.J. Brown:** Funding acquisition, Writing - review & editing. **Y.U. Sharif:** Software, Writing - review & editing.

Declaration of Competing Interest

The authors declare that they have no known competing financial interests or personal relationships that could have appeared to influence the work reported in this paper.

References

Al-Defae, A.H., Caucis, K., Knappett, J.A., 2013. Aftershocks and the whole-life seismic performance of granular slopes. Géotechnique 63 (14), 1230–1244. https://doi.org/10.1680/geot.12.P.149.

Arroyo, M., Butlanska, J., Gens, A., Calvetti, F., Jamiolkowski, M., 2011. Cone penetration tests in a virtual calibration chamber. Geotechnique 61 (6), 525–531. https://doi.org/10.1680/geot.9.P.067.

Badakhshan, E., Noorzad, A., Bouazza, A., Zameni, S., King, L., 2020. A 3D-DEM investigation of the mechanism of arching within geosynthetic-reinforced piled embankment. Int. J. Solids & Struct. 187, 58–74. https://doi.org/10.1016/j.ijsolstr.2019.03.035. Elsevier Ltd.

Bradshaw, A. S., Zuelke, R., Hildebrandt, L., Robertson, T. and Mandujano, R. (2018) Physical modelling of a helical pile installed in sand under constant crowd, in Davidson, C., Knappett, J. A., Brown, M. J., Brennan, A. J., Augarde, C., Coombs, W., Wang, L., Richards, D., White, D., and Blake, A. (eds) Proceedings of the 1st International Symposium on Screw Piles for Energy Applications (ISSPEA). Dundee, UK, pp. 109–115. doi: https://doi.org/10.20933/100001123.

BS8004:2015 (2015) Code of practice for foundations. BSI Standards Limited.

Byrne, B.W., Houlsby, G.T., 2015. Helical piles: An innovative foundation design option for offshore wind turbines. Philos. Trans. Royal Soc. A: Math., Phys. & Eng. Sci. 373 (2035), 1–11. https://doi.org/10.1098/rsta.2014.0081.

Cerfontaine, B., Brown, M.J., Knappett, J.A., Davidson, C., Sharif, Y.U., Huisman, M., Ottolini, M., Ball, J.D., 2021. Control of screw pile installation to optimise performance for offshore energy applications. Géotechnique.

Cerfontaine, B., Knappett, J., Brown, M.J., Davidson, C., Al-Baghdadi, T., Brennan, A., Augarde, C., Coombs, W., Wang, L., Blake, A., Richards, D., Ball, J., 2020. A Finite Element approach for determining the full load-displacement relationship of axially-loaded screw anchors, incorporating installation effects. Can. Geotech. J. https://doi.org/10.1139/cgj-2019-0548.

Chen, Y., Deng, A., Wang, A., Sun, H., August 2018. Performance of screw–shaft pile in sand: Model test and DEM simulation. *Comput. Geotech.* 104, 118–130. https://doi.org/10.1016/j.compgeo.2018.08.013. Elsevier.

Choi, Y., Kim, D.-C., Kim, S.-S., Nam, M.S., Kim, T.-H., 2013. Implementation of Noise-Free and Vibration-Free PHC Screw Piles on the Basis of Full-Scale Tests. J. Construction Eng. & Manage. 139 (8), 960–967. https://doi.org/10.1061/(asce)co.1943-7862.0000667.

Ciantia, M.O., Arroyo, M., Butlanska, J., Gens, A., 2016. DEM modelling of cone penetration tests in a double-porosity crushable granular material. Comput. & Geotec. 73, 109–127. https://doi.org/10.1016/j.compgeo.2015.12.001. Elsevier Ltd.

Ciantia, M. O., Boschi, K., Shire, T. and Emam, S. (2018) Numerical techniques for fast generation of large discrete-element models, Proceedings of the Institution of Civil Engineers - Engineering and Computational Mechanics, 171(4), pp. 147–161. doi: 10.1680/jencm.18.00025.

Ciantia, M. O., O'Sullivan, C. and Jardine, R. J. (2019) Pile penetration in crushable soils : Insights from micromechanical modelling, in Proceedings of the XVII ECSMGE-2019. Reykjavik, Iceland, Iceland, pp. 298–317. doi: 10.32075/17ECSMGE-2019-1111.

Coetzee, C. J. (2019) Particle upscaling: Calibration and validation of the discrete element method, Powder Technology. Elsevier B.V., 344, pp. 487–503. doi: 10.1016/j.powtec.2018.12.022.

Da Cruz, F., Emam, S., Prochnow, M., Roux, J.N., Chevoir, F., 2005. Rheophysics of dense granular materials: Discrete simulation of plane shear flows. Phys. Rev. E - Statistical, Nonlinear, and Soft Matter Phys. 72 (2), 1–17. https://doi.org/10.1103/PhysRevE.72.021309.

Davidson, C., Brown, M. J. M. J., Cerfontaine, B., Al-Baghdadi, T., Knappett, J., Brennan, A., Augarde, C., Coombs, W., Wang, L., Blake, A., Richards, D. and Ball, J. D. (2020) Physical modelling to demonstrate the feasibility of screw piles for offshore jacket-supported wind energy structures, Géotechnique, pp. 1–19. doi: 10.1680/jgeot.18.p.311.

Dong, Y., Fatahi, B., Khabbaz, H. and Kamruzzaman, A. H. M. (2018) Investigating Effects of Particle Scaling for Cavity Expansion Simulation Using Discrete Element Method, Proceedings of GeoShanghai 2018 International Conference: Fundamentals of Soil Behaviours, pp. 938–946. doi: 10.1007/978-981-13-0125-4_104.

Garnier, J., Gaudin, C., Springman, S.M., Culligan, P.J., Goodings, D., Konig, D., Kutter, B., Phillips, R., Randolph, M.F., Thorel, L., et al., 2007. Catalogue of scaling laws and similitude questions in geotechnical centrifuge modelling. Int. J. Phys. Model. Geotech. 7 (3), 01–23. https://doi.org/10.1680/ijpmg.2007.070301.

Giampa, J.R., Bradshaw, A.S., Schneider, J.A., 2017. Influence of Dilation Angle on Drained Shallow Circular Anchor Uplift Capacity. Int. J. Geomech. 17 (2), 4016056. https://doi.org/10.1061/(ASCE)GM.1943-5622.0000725.

Hao, D., Wang, D., O'Loughlin, C.D., Gaudin, C., 2019. Tensile monotonic capacity of helical anchors in sand: interaction between helices. Can. Geotech. J. 56 (10), 1534–1543. https://doi.org/10.1139/cgj-2018-0202.

Harnish, J., El Naggar, H.M., February 2017. Large Diameter Helical Pile Capacity - Torque Correlations. Can. Geotech. J. 986, 1–51. https://doi.org/10.1139/cgj-2016-0156.

Itasca Consulting Group (2019) PFC3D 6.17.

Janda, A., Ooi, J.Y., 2016. DEM modeling of cone penetration and unconfined compression in cohesive solids. Powder Technol. 293, 60–68. https://doi.org/10.1016/j.powtec.2015.05.034. Elsevier B.V.

Khosravi, A., Martinez, A., DeJong, J., 2020. DEM simulations of CPT measurements and soil classification. Can. Geotech. J. 57 (9) https://doi.org/10.1139/cgj-2019-0512.

Khoubani, A., Evans, T.M., 2018. An efficient flexible membrane boundary condition for DEM simulation of axisymmetric element tests. Int. J. Numer. Anal. Meth. Geomech. 42 (4), 694–715. https://doi.org/10.1002/nag.v42.410.1002/nag.2762.

Komatsu, A. (2007) Development on battered pile with screw pile method (NS-ECO pile), in Kikuchi, Y., Otani, J., Kimura, M., and Morikawa, Y. (eds) Proceedings of the International Workshop on recent advances of deep foundations (IWDPF07). Yokosuka, Japan.

Lauder, K., 2010. The performance of pipeline ploughs. University of Dundee, UK.

Lauder, K.D., Brown, M.J., Bransby, M.F., Boyes, S., 2013. The influence of incorporating a forecutter on the performance of offshore pipeline ploughs. Appl. Ocean Res. 39, 121–130. https://doi.org/10.1016/j.apor.2012.11.001. Elsevier Ltd.

Lommen, S., Mohajeri, M., Lodewijks, G., Schott, D., 2019. DEM particle upscaling for large-scale bulk handling equipment and material interaction. Powder Technology. 352, 273–282. https://doi.org/10.1016/j.powtec.2019.04.034. The Authors.

Lopera Perez, J. C., Kwok, C. Y., O'Sullivan, C., Huang, X. and Hanley, K. J. (2016) Assessing the quasi-static conditions for shearing in granular media within the critical state soil mechanics framework, Soils and Foundations. Elsevier, 56(1), pp. 152–159. doi: 10.1016/j.sandf.2016.01.013.

Lutenegger, A.J., 2011. Historical Development of Iron Screw-Pile Foundations: 1836–1900, *The International Journal for the History of*. Eng. Technol. 81 (1), 108–128. https://doi.org/10.1179/175812109x12547332391989.

McDowell, G.R., Falagush, O., Yu, H.S., 2012. A particle refinement method for simulating DEM of cone penetration testing in granular materials. Geotechnique Lett. 2 (7–9), 141–147. https://doi.org/10.1680/geolett.12.00036.

O'Sullivan, C. (2011) Particulate Discrete Element Modelling, Particulate Discrete Element Modelling. Spon Press. doi: 10.1201/9781482266498.

Otsubo, M., O'Sullivan, C., Shire, T., 2017. Empirical assessment of the critical time increment in explicit particulate discrete element method simulations. Comput. Geotech. 86, 67–79. https://doi.org/10.1016/j.compgeo.2016.12.022.

Perko, H. A. (2009) Helical Piles. A practical guide to design and installation. 1st Edit. John Wiley & Sons, Inc. doi: 10.1002/9780470549063.

Schiavon, J. A., Tsuha, C. H. C., Neel, A. and Thorel, L. (2016a) Physical modelling of a single-helix anchor in sand under cyclic loading, EUROFUGE 2016 3rd European conference on Physical Modelling in Geotechnics, (June), pp. 275–279.

Schiavon, J. A., Tsuha, C. H. C. and Thorel, L. (2016b) Scale effect in centrifuge tests of helical anchors in sand, International Journal of Physical Modelling in Geotechnics, 16(4), pp. 185–196. doi: 10.1680/jphmg.15.00047.

Sharif, Y.U., Brown, M.J., Cerfontaine, B., Davidson, C., Ciantia, M., Knappett, J., Brennan, A., Ball, J.D., Augarde, C., Coombs, W., Blake, A., Richards, D., White, D., Huisman, M., Ottolini, M., 2020a. Effects of screw pile installation on installation requirements and in-service performance using the Discrete Element Method. Can. Geotech. J. (published online). https://doi.org/10.1139/cgj-2020-0241.

Sharif, Y.U., Brown, M.J., Ciantia, M.O., Cerfontaine, B., Davidson, C., Knappett, J., Meijer, G.J., Ball, J., 2020b. Using DEM to create a CPT based method to estimate the installation requirements of rotaty installed piles in sand. Canadian Geotechnical Journal (published online). https://doi.org/10.1139/cgj-2020-0017.

Sharif, Y. U., Brown, M. J., Ciantia, M. O., Knappett, J. A., Davidson, C., Cerfontaine, B., Robinson, S., B., C., Robinson, S. and Ball, J. (2019) Numerically modelling the installation and loading of screw piles using DEM, in Proceedings of the 1st International Symposium on Screw Piles for Energy Applications. Dundee, UK.

Shi, D., Yang, Y., Deng, Y., Xue, J., 2019. DEM modelling of screw pile penetration in loose granular assemblies considering the effect of drilling velocity ratio. Granular Matter. 21 (3), 74. https://doi.org/10.1007/s10035-019-0933-3.

Shire, T., Hanley, K. J. and Stratford, K. (2020) DEM simulations of polydisperse media: efficient contact detection applied to investigate the quasi-static limit, Computational Particle Mechanics. Springer International Publishing. doi: 10.1007/s40571-020-00361-2.

Spagnoli, G., Hollanda, C. De, Tsuha, C., 2020. A review on the behavior of helical piles as a potential offshore foundation system, *Marine Georesources & Geotechnology*. Taylor & Francis 1–24. https://doi.org/10.1080/1064119X.2020.1729905.

Stanier, S. A., Black, J. A. and Hird, C. C. (2014) Modelling helical screw piles in soft clay and design implications, Proceedings of the Institution of Civil Engineers: Geotechnical Engineering, 167(5), pp. 447–460. doi: 10.1680/geng.13.00021.

Tan, S.C., Duan, L.C., Tan, S.E., Shi, H., 2011. Study on Critical Drilling Parameters for Auger Drilling. Adv. Mater. Res. 243–249, 3331–3340. https://doi.org/10.4028/www.scientific.net/amr.243-249.3331.

Tang, C., Phoon, K.-K., 2020. Statistical evaluation of model factors in reliability calibration of high displacement helical piles under axial loading. Can. Geotech. J. 57 (2), 246–262. https://doi.org/10.1139/cgj-2018-0754.

Ting, J.M., Corkum, B.T., Kauffman, C.R., Greco, C., 1989. Discrete numerical model for soil mechanics. J. Geotech. Eng. 115 (3), 379–398.

Tsuha, C.H.C., Aoki, N., 2010. Relationship between installation torque and uplift capacity of deep helical piles in sand. Can. Geotech. J. 47 (1), 635–647. https://doi.org/10.1139/T09-128.

Wang, L., Zhang, P., Ding, H., Tian, Y., Qi, X., 2020. The uplift capacity of single-plate helical pile in shallow dense sand including the influence of installation. *Mar. struct.*. Elsevier Ltd 71, 102697. https://doi.org/10.1016/j.marstruc.2019.102697.

White, D.J., Bolton, M.D., 2004. Displacement and strain paths during plane-strain model pile installation in sand. Geotechnique 54 (6), 375–397. https://doi.org/10.1680/geot.2004.54.6.375.

Yang, J., 2006. Influence zone for end bearing of piles in sand. J. Geotech. Geoenviron. Eng. 132 (9), 591–602. https://doi.org/10.1061/(ASCE)1090-0241(2006)132.

Yu, H.-S., 2000. Cavity Expansion Methods in Geomechanics. Springer Sci. & Business Media. https://doi.org/10.1017/CBO9781107415324.004.

Zhang, N., Evans, T.M., 2019. Discrete numerical simulations of torpedo anchor installation in granular soils. Comput. Geotech. 108 (April), 40–52. https://doi.org/10.1016/j.compgeo.2018.12.013. Elsevier.

Zhang, Z., Wang, Y.H., 2015. Three-dimensional DEM simulations of monotonic jacking in sand. Granular Matter. 17 (3), 359–376. https://doi.org/10.1007/s10035-015-0562-4.